END
DATE
FILMED

DTIC

MICROCOPY RESOLUTION TEST CHART

NATIONAL BUREAU OF STANDARDS-1963-A

ELECTROMAGNETIC WAVES NEAR DIELECTRIC STRUCTURES

Final Report

by

G. Tricoles
E. L. Rope
R. A. Hayward

Prepared for U. S. Naval Air Systems Command

Under

Contract N00019-81-C-0389

GENERAL DYNAMICS
Electronics Division

DTIC
ELECTE
SEP 19 1983
D

83 09 02 012

ELECTROMAGNETIC WAVES NEAR DIELECTRIC STRUCTURES

Final Report

by

G. Tricoles
E. L. Rope
R. A. Hayward

Prepared for U. S. Naval Air Systems Command

Under

Contract N00019-81-C-0389

GENERAL DYNAMICS
Electronics Division
P. O. Box 85227, San Diego, California 92138 • 5227 • 619-573-6111

REPORT DOCUMENTATION PAGE		READ INSTRUCTIONS BEFORE COMPLETING FORM
1. REPORT NUMBER	2. GOVT ACCESSION NO.	3. RECIPIENT'S CATALOG NUMBER
4. TITLE (and Subtitle)		5. TYPE OF REPORT & PERIOD COVERED
Electromagnetic Waves Near Dielectric Structures		Final Sept. 1981 - June 1983
		6. PERFORMING ORG. REPORT NUMBER R-83-047
7. AUTHOR(s)		8. CONTRACT OR GRANT NUMBER(s)
G. Tricoles, E. L. Rope, R. A. Hayward		N00019-81-C-0389
9. PERFORMING ORGANIZATION NAME AND ADDRESS		10. PROGRAM ELEMENT, PROJECT, TASK AREA & WORK UNIT NUMBERS
General Dynamics Electronics Division P.O. Box 81127 San Diego, CA 92128		NONE
11. CONTROLLING OFFICE NAME AND ADDRESS		12. REPORT DATE
U. S. Naval Air Systems Command, AIR-33R Washington, D.C. 20361		Feb. 1983
		13. NUMBER OF PAGES 72
14. MONITORING AGENCY NAME & ADDRESS(if different from Controlling Office)		15. SECURITY CLASS. (of this report)
NONE		NONE Unclassified
		15a. DECLASSIFICATION. DOWNGRADING SCHEDULE NONE
16. DISTRIBUTION STATEMENT (of this Report)		
NONE APPROVED FOR PUBLIC RELEASE DISTRIBUTION UNLIMITED		
17. DISTRIBUTION STATEMENT (of the abstract entered in Block 20, if different from Report)		
NONE		
18. SUPPLEMENTARY NOTES		
NONE		
19. KEY WORDS (Continue on reverse side if necessary and identify by block number)		
Wave Propagation, radomes, antennas, integrated optics		

20. ABSTRACT (Continue on reverse side if necessary and identify by block number)

The influence of radome boresight error on missile guidance motivates the need for accurate methods of analyzing radomes. Although methods based on aperature diffraction and the approximation of local planeness are useful in some cases, these methods are inadequate for small radomes. This report describes a new method. It compares theoretical and experimental wavefront data.

DD FORM 1473 EDITION OF 1 NOV 65 IS OBSOLETE
1 JAN 73

CONTENTS

ILLUSTRATIONS

ILLUSTRATIONS (Continued)

ILLUSTRATIONS (Continued)

TABLES

1. INTRODUCTION

This report describes a project that investigated the field distributions produced by incident electromagnetic waves near dielectric structures. The structures are flat slabs, hollow slabs, hollow cylinders, and hollow cones, all with finite dimensions. The structures are idealized but are realistic models for analyzing the electromagnetic effects that occur near practical radome configurations. Because wave polarization direction strongly influences radome boresight error, the project emphasizes the polarization dependence of wavefront distortions. The work in the project dealt with two approximations commonly made in analyzing radomes: (1) treat the radome as locally flat by approximating its transmittance as that of an assembly of infinitely broad dielectric sheets; (2) omit guided waves.

Radomes produce several electromagnetic effects. The simplest are reflection and refraction, which involve essentially plane waves. In addition, radome edges or vertices scatter non-plane waves. Finally, radomes generate guided waves, with propagation constants that differ from those of free-space waves. These effects depend on the radome configuration, and the frequency, polarization, and direction of the incident wave. For a coherent externally incident wave, the distinct radome-generated waves are coherent; they interfere to produce a complicated field distribution near the radome. The practical consequences are boresight error, attenuation, and increases in sidelobe levels. Consequently, radomes strongly influence missile guidance. Moreover, radome effects depend on temperature, which increases nonuniformly in flight.

The effects of radomes on electromagnetic waves motivated this research. The project had two goals. One was to provide a physical basis for numerical radome analysis that describes the complicated fields near radomes in terms of simpler constituent waves, analogous to geometric diffraction theory, which has been developed mainly for metallic scatterers. The other goal was to develop a new guidance concept that utilizes antennas embedded in dielectrics; this approach is analogous to integrated optics. The two goals are closely related because one seeks to understand guided waves on finite structures and the other seeks to exploit the guided waves.

Our approach involved theory, computation, and experiment. The theory includes a diffraction theory, with integration over a Huygens surface, and a generalization of the moment method which has been developed by J. Richmond for dielectrics. The experiments involved probing the complex-valued field in a radome-bounded region with a small antenna to evaluate transmittance and identify constituent fields from their interference patterns, and then comparing measured and computed values.

Section 2 of this report describes radome boresight error and surveys some analytical methods that are approximate. It describes the validity of the methods and describes omissions in them; specifically, guided waves and a local flat sheet approximation are significant. Polarization also is a variable. This section describes an integrated antenna-radome concept that exploits guided waves and refracted waves on dielectric slabs.

Section 2 also gives a new moment method theory for hollow curved shells, like cones. This theory is based on Richmond's vector and potental formulation, but it is new because it develops closed form expression for matrix elements of doubly-curved hollow shells rather than cylinders.

To connect moment method theory and radome problems, Section 3 first gives numerical results for slabs and hollow wedges. Analysis of slab data shows that guided waves are excited. Analysis of wedge data predicts boresight error properties, especially polarization dependence of the algebraic sign of error. This polarization dependence was observed in measurements made for an axially symmetric, pointed radome; data are given in paragraph 3.4. In addition for plane wave incidence, wavefront phase and intensity were measured in the region bounded by the axially symmetric shell. The measured wavefront data were compared with values computed by a surface integration method. Discrepancies between these calculations and measurements were shown to be caused by omitting a guided wave.

Section 4 describes measurements and calculations for fields behind a hollow finite cylinder. The new moment method was used. Two formulations were compared. One included only radial field components. The other included axial and radial. Discrepancies between calculation and measurements were smaller when both radial and axial components were used.

Section 5 described experiments and moment method results for a hollow cone. Accuracy was greater when both axial and radial fields were used.

2.   ANALYSIS

Radomes reduce missile guidance accuracy by causing boresight error, which is an error in the direction of a wave source, either an emitter or a reflector. Although progress has been made in analyzing boresight error, most methods are approximate, so they are accurate for some configurations but not for others. Unfortunately extensive tests of accuracy are lacking.

Relatively simple methods are adequate if the radome-enclosed antenna is an order of magnitude larger than the wavelength (References 1 and 2). For example, consider the direct ray method shown in Figure 2-1. Propagation to an observation point in the radome-bounded region is described by a single ray through the point and the radome where the ray intersects the radome. Transmittance for the ray is that of a flat sheet that depends on position and incidence direction. The transmittance is the ratio of the complex-valued field amplitude with a dielectric structure present to that of the incident field.

For antennas with a diameter of about five wavelengths the direct ray method is inadequate. Accurate boresight error was calculated, however, by integrating over an incident wavefront, a Huygens surface. Again the transmittance was that of flat sheets, but for converging rays, as in Figure 2-2. For antennas with apertures approximately a wavelength in size, like broadband antennas, surface integration gives marginal accuracy. See Reference 3.

ANB050A
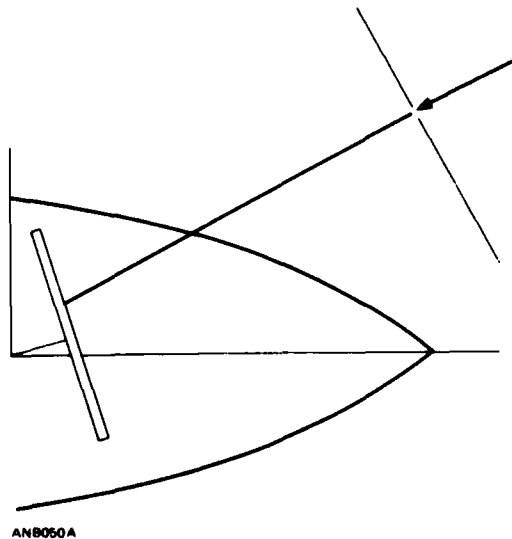
Figure 2-1. The Direct Ray Method. A single incident wave normal
(or ray) is associated with a point on the receiving aperture.
The radome is a surface of revolution, but only
a plane is sketched

2-1
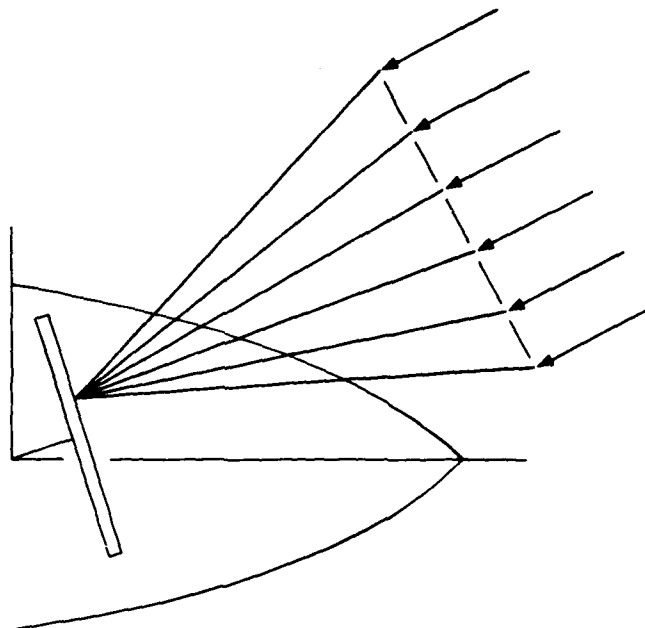
ANB009

Figure 2-2. Surface Integration Method. The radome is a surface of revolution.
Integration is over a portion of the incident wavefront.

To evaluate the accuracy of analytical methods, measured and computed boresight errors
can be compared, but the enclosed antenna integrates over its extent and obscures
transmittance. Moreover, experiments with specific antennas lack generality. The
influence of aperture size can be minimized however, by probing the wavefront in the
radome-bounded region with a small antenna. Proving gives explicit data on the
transmittance over a small region and directly tests the propagation description and its
approximations. See References 2 and 3.

The transmittance depends on the wave mechanisms present. Direct rays and converging
rays correspond to plane waves with free space propagation constants. Edges and
vertices give approximately cylindrical and spherical waves, again with free space
propagation constants. In addition, dielectric structures support guided waves. The
influence of guided wave amplitudes, which decrease exponentially with distance from an
infinite slab, are slight for antennas that are reasonably large. However, guided waves
seem significant for small, broadband antennas. See Reference 3. In addition, guided
waves have potential for new systems with antennas embedded in radomes, in analogy to
integrated optics.

2-2

INCIDENCE

α

REFLECTED

GUIDED

REFRACTED

TRANSMITTED

AHR-001
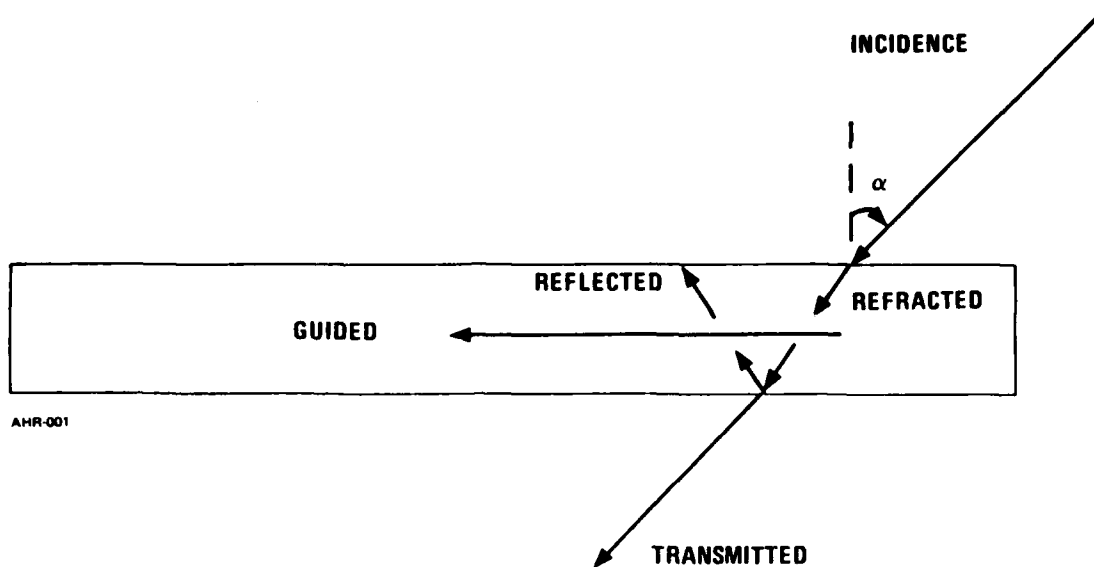
Figure 2.1-1. Waves on a Slab

2.1   GUIDED WAVES; A NEW APPROACH TO GUIDANCE AND DIRECTION FINDING

The new approach consists of an array of self-referencing interferometers (References 3 and 4).   A self-referencing interferometer consists of a dielectric slab and a set of antenna elements distributed over the slab. The interferometer operates because a wave incident on a slab excites guided waves as well as reflected and refracted waves, as shown in Figure 2.1-1. The guided waves have propagation constants that differ from those of the other waves, so an interference fringe pattern is formed (Figure 2.1-2). The maxima of intensity are chosen as locations for sensing antennas because the gain of the antenna is an order of magnitude greater than that of the antenna in free space. Because the location of maxima depends on frequency, several distinct antennas, each for limited frequency ranges, can be utilized.

INTENSITY

δS

SLAB

AHR 002

$$\delta S = 2\pi/(K_g - K_o \sin \alpha)$$
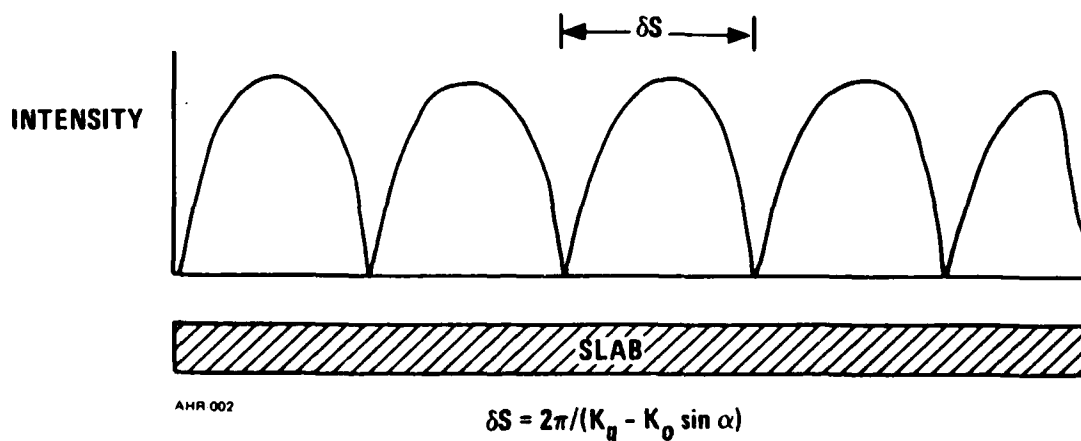
Figure 2.1-2. Intensity Fringes Are Formed Near a Slab

2-3
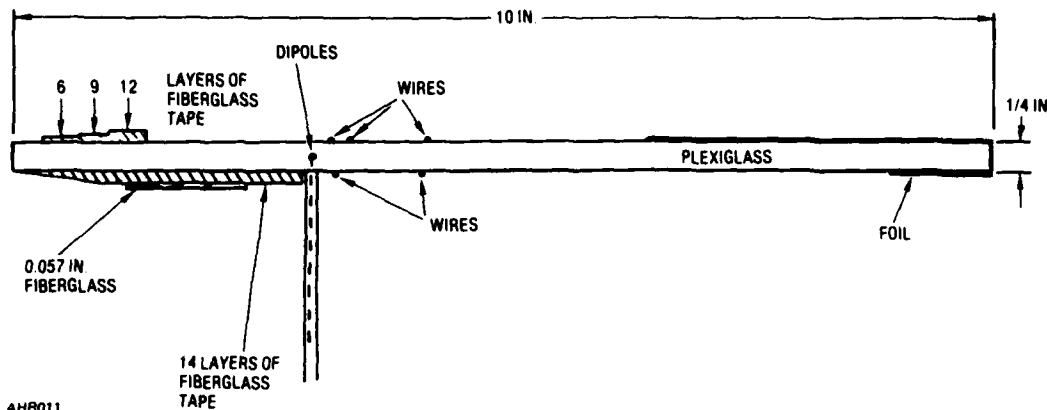
Figure 2.1-3. Antennas Embedded in a Nonuniformly Thick Slab

In an earlier project, we analyzed the fringe patterns for flat slabs with the moment method. We fabricated an interferometer on a slab (Figure 2.1-3) and measured the farfield radiation pattern (Figure 2.1-4). The computed pattern is shown in Figure 2.1-5. We also combined two interferometers to form a hollow wedge and measured the sum and difference patterns for a monopulse arrangement (Figures 2.1-6 and 2.1-7). The deep minimum in the difference pattern is in the plane of the slab. For an axially symmetric structure, interferometers would be arranged as in Figure 2.1-8.

The earlier project emphasized transverse electric fields or perpendicular polarization. In this project we extended analysis to include parallel polarization for transverse magnetic waves on slabs and investigate axially symmetric radomes.

2.2 MOMENT METHOD

The moment method procedure for slabs and hollow wedges was described in General Dynamics Electronics Division Report R-81-125 (Reference 5); it is based on a theory originated by Richmond (References 6 and 7) wherein a finite slab is represented by a finite number of infinitely long cylinders called cells. An integral equation represents the total field E^T, where E^T is the sum of the incident and scattered field E^I and E^S,

$$E^T = E^I + E^S \tag{2-1}$$

The scattered field, from a vector potential A and a scalar potential Φ, is

$$E^S = i\omega A - \nabla'\Phi, \tag{2-2}$$

2-4
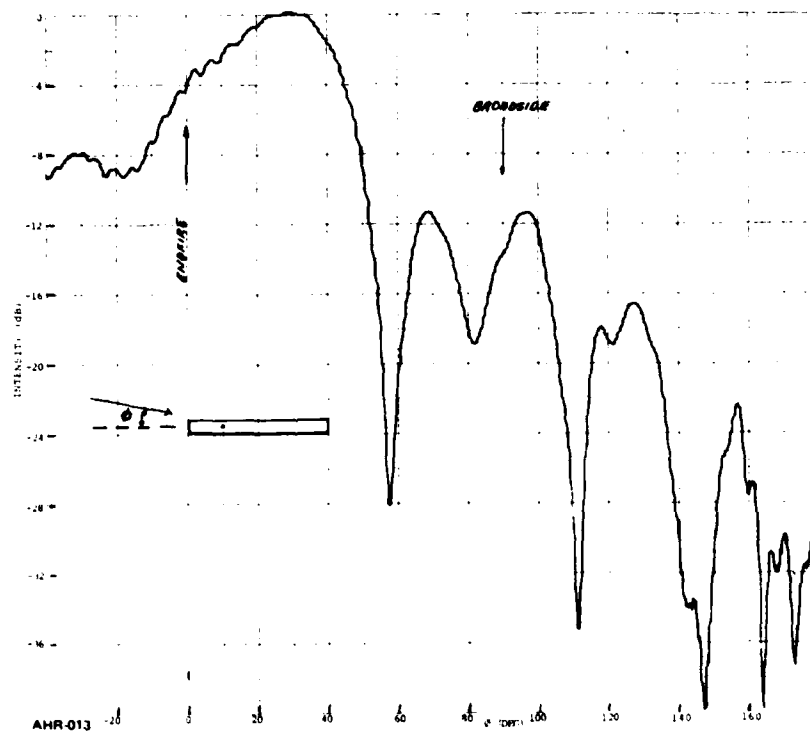
Figure 2.1-4. Intensity for Two, Colinear Dipoles in Nonuniform Slab.
Frequency 9.4 GHz.
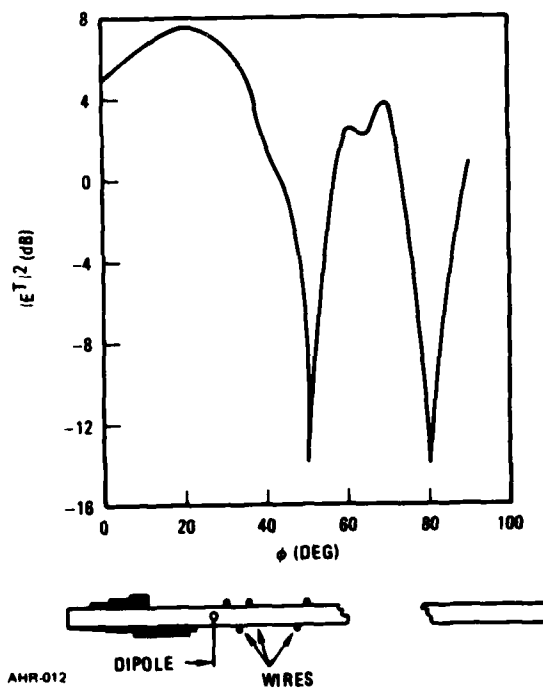
Figure 2.1-5. Computed Field in a Quarter-Inch Tapered Slab with Wires and
Dipole, at Location of Dipole

2-5
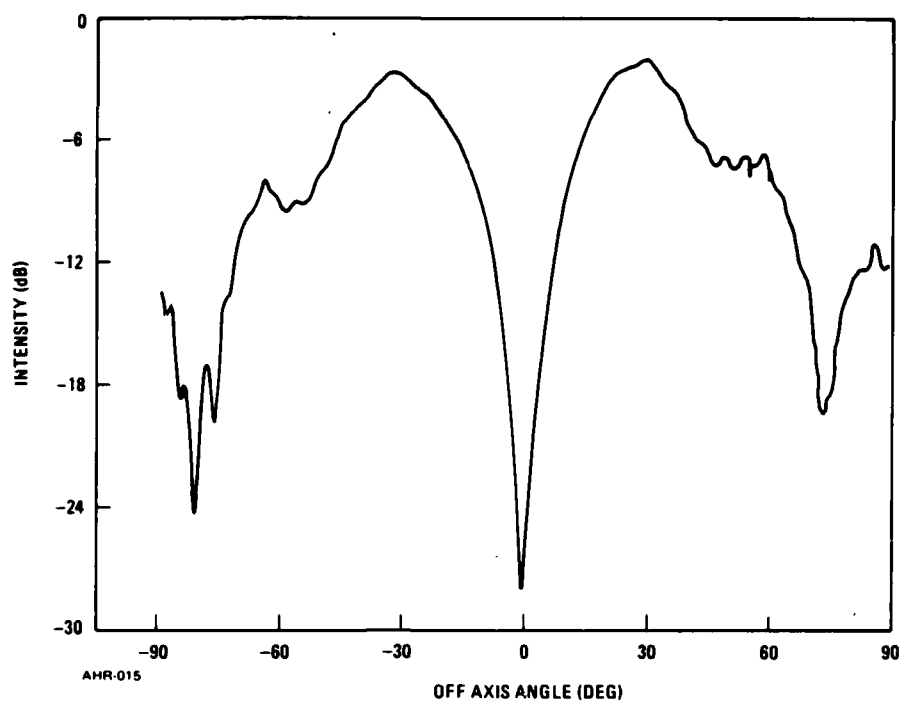
Figure 2.1-6. Difference Mode Pattern for Two Interferometers Formed into a Wedge. Frequency 9.4 GHz. The off-axis angle is measured from the symmetry axis of the wedge.
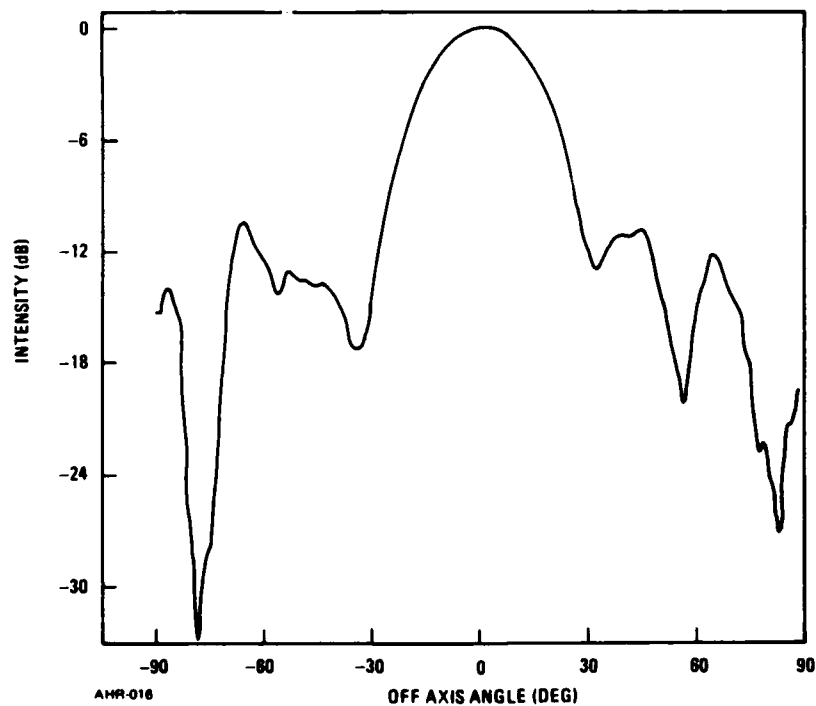
Figure 2.1-7. Sum Mode Pattern Formed by Two Interferometers Formed into a Wedge. Each slab tapered thickness and had two colinear dipoles on its surface.

2-6
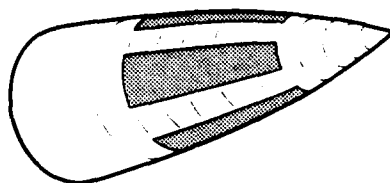
(a) INTERFEROMETERS ON MISSILE NOSE
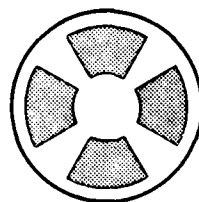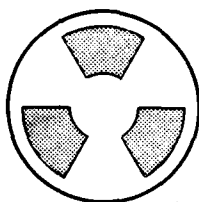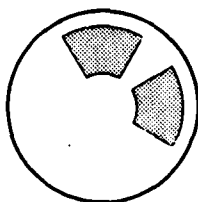
(b) TWO INTERFEROMETERS   (c) THREE INTERFEROMETERS   (d) FOUR INTERFEROMETERS

AHR-017

Figure 2.1-8. Installations of Self-Referencing Interferometers on
Missile Nose. The interferometers in (b) can be diametrically
opposite for a rolling airframe.

where i is $\sqrt{-1}$, ω is the radian frequency, and time dependence is exp(-iωt). The prime indicates that the gradient is taken at the observation point. The vector potential is

$$4\pi A = -i\omega\mu_0 E_0 \int (\kappa-1)g \, E^T \, dv, \qquad (2-3)$$

where κ is dielectric constant, g is r^{-1} exp(ikr), k equals $2\pi/\lambda$, λ is wavelength, and r is the distance between the integration and observation points. The scalar potential is

$$4\pi\Phi = - \int g\nabla.(\kappa-1) \, E^T \, dv \qquad (2-4)$$

Equation (2-1) is an integral equation. It is reduced to a set of simultaneous equations by decomposing the scatterer into elementary cells that are small enough to justify assuming E^T constant in each cell. From Equations (2-1) and (2-2) we obtain the set of simultaneous equations, as follows. For a typical cell, which is labeled with index m, we enforce the integral equation. Therefore, at the center of each cell,

$$E_m^T - E_m^S = E_m^I \qquad (2-5)$$

2-7

The index m ranges from 1 through N, where N is the number of cells. E_m^S is a sum because all cells contribute to the field at any one cell. Therefore, we revise the notation, so

$$E_m^T - E_{mn}^S = E_m^I \qquad (2\text{-}6)$$

The integrals for Equation (2-2) were evaluated in Reference 5 on the assumption that E^T is transverse. In the coordinate system of Figure 2.2-1, the assumption for transverse fields is that the longitudinal or z component E_z is zero. This section generalizes the analysis of Reference 5, giving the fields that result when both E_x and E_z are included and assumed nonzero. We present only the results here since the basic derivations are contained in Reference 5. The derivations with E_z not zero are similar but somewhat more involved, and the gradient operation introduces additional terms, which can be described as a coupling of field components.

We consider dielectric rings as in Figure 2.2-1. A set of rings with distinct radii generates a hollow cone, and a set of rings with equal radii generates a finite cylinder. The coordinate system and terminology of Figure 2.2-2 are used in the following discussion.
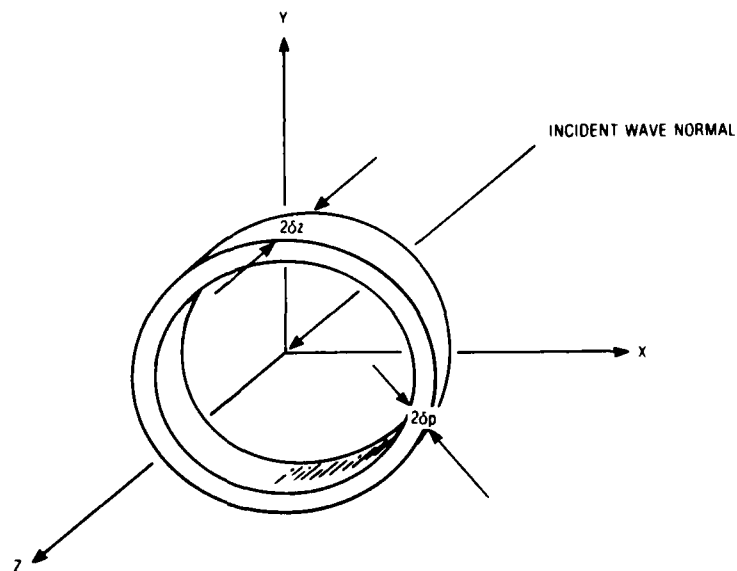
ADR002

Figure 2.2-1. Dielectric Ring and Coordinate System
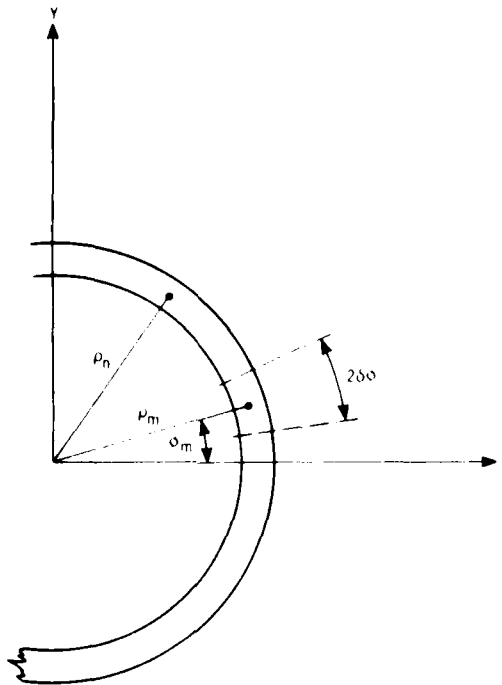
Figure 2.2-2. Coordinates for a Cell. A typical Cell has Dimensions:
Radial $2\delta\rho$, Circumferential $2\delta\phi$, and Longitudinal $2\delta z$

2.2.1 SCATTERED FIELD FOR DIAGONAL ELEMENTS

2.2.1.1 VECTOR POTENTIAL — The scattered field at cell m produced by the vector potential within cell m is

$$E_{Am}^{s} = 2(\kappa-1)\left\{ i\frac{2}{\pi}k\,\delta z\,\delta\rho\rho_m\,\delta\phi - \frac{\rho_m}{12\pi\delta z^2}\,\delta\rho\,\delta\phi s_2^2 \right.$$

$$\left. + \frac{s^2}{4}\left[1 - \log(s_2/2\,\delta z)^2\right] \right\} E_m^T \tag{2-7}$$

where

$$s_2^2 = \delta\rho^2 + \rho_m^2\,\delta\phi^2$$

Equation (2-7) is Equation (2-39) of Reference 5. The expression for the diagonal terms is identical to that for $E_z = 0$. Of course, Equation (2-7) is a vector equation. That is, Equation (2-7) applies to E_x and E_z.

2-9

2.2.1.2 SCALAR POTENTIAL — The x and y components of the scattered field are

$$E_{xm}^S = (1-\kappa) \left\{ \frac{\delta\phi^2}{2} \left[1 + (1-\ln q_1)(1-q_2) + q_3 \right] \cos^2\phi_m \right.$$

$$+ \left(\frac{s}{2\rho_m} \right)^2 \left[(1-\ln q_1) + q_3 \right] \sin^2\phi_m \left. \right\} E_{xm}^T$$

$$- \frac{4i}{\lambda\pi} (\kappa-1) t_s \delta\rho\delta\phi \cos\phi_m E_{zm}^T, \tag{2-8}$$

$$E_{ym}^S = - \frac{4i}{\lambda\pi} (\kappa-1) t_s \delta\rho\delta\phi \sin\phi_m E_{zm} \tag{2-9}$$

where t_s is $\delta\rho/\cos\alpha$, α is the half angle of the cone if the scatterer is a cone, q_1 is $(s/2\delta z)^2$, q_2 is $\frac{1}{2}(s/\rho_m\delta\phi)^2$, and q_3 is $(\delta\rho\rho_m\delta\phi)/3\pi\delta z^2$. Equation (2-8) states that E_{xm}^S is affected by E_{zm}^T.

2.2.2 SCATTERED FIELD FOR OFF-DIAGONAL ELEMENTS

2.2.2.1 VECTOR POTENTIAL — The vector potential of cell n generates a scattered field x component at cell m as follows:

$$E_{Axm}^S = \frac{2}{\pi} (\kappa-1) k^2\delta\rho\delta\phi\delta z \, \rho_n \frac{e^{ikB}}{B} \, \text{sinc}(kb\delta\rho B^{-1}) \, \text{sinc}\left[kB^{-1}(z_n-z_m)\delta z \right] E_{xn}^T \tag{2-10}$$

where sinc z is $(z^{-1}\sin z)$, b is $\left[\rho_n-\rho_m\cos(\varphi_n-\varphi_m) \right]$, and

$$B = \left[\rho_n^2 + \rho_m^2 - 2\rho_n\rho_m \cos(z_n-z_m) + (z_n-z_m)^2 \right]^{1/2} \tag{2-11}$$

The z component, due to A, is also given by Equation (2-10) with E_{xn}^T replaced by E_{zn}^T.

2.2.2.2 SCALAR POTENTIAL — The scalar potential generates an x component at cell m due to the nth cell as follows:

$$E_{xm}^S = \frac{2}{\pi} (\kappa-1)\delta\rho\delta\phi\delta z \cos\phi_n e^{ikB} B^{-2}x$$

2-10

$$\Big\} 2(B^{-1}-ik)\,c \;+\; ik\rho_n\Big[(2B^{-1}-ik)B^{-1}\,bc \quad \cos\phi_n\Big]\Big\} E^T_{xn}$$

$$+\;(\kappa-1)\frac{2i}{\pi}\,\delta\rho\,\delta\phi\,t_s\,k\rho_n\,e^{ikB}\,B^{-2}\,\Big\} z_{mn}(ik-2B^{-1})B^{-1}\,c\,\cos\phi_m$$

$$+\;z_{mn}\,(ik-2B^{-1})\rho_n B^{-1}\,\sin(\phi_n-\phi_m)\,\sin\phi_n\,\Big\} E^T_{zn} \tag{2-12}$$

where c is $\rho_m\cos\phi_m-\rho_n\cos\phi_n$, and z_{mn} is z_m-z_n.

The z component is

$$E^S_{zm} \;=\; (\kappa-1)\frac{2i}{\pi}\delta\rho\,\delta\phi\,t_s k\rho_n\,e^{ikB}\,B^{-2}\Big[1-(ik-2B^{-1})z_{mn}\,z_{nm}\,B^{-1}\Big]E_{zn}$$

$$+\;(\kappa-1)\frac{2}{\pi}\delta\rho\,\delta\varphi\,\delta z\,\cos\phi_n\,\Big\}-ik\rho_n b\,(2B^{-1}-ik)B^{-1}-(B^{-1}-ik)\Big\} z_{nm}\,e^{ikB}B^{-2}\,E_{xn}. \tag{2-13}$$

3. DIELECTRIC SLAB, WEDGE, AND SHELL

The wedge and slabs described in the following sections were analyzed because they have no curvature and introduce effects caused by finite structures. These effects are guided waves, edge-scattered waves, and polarization dependence. Wedges can be analyzed by a moment method that is rigorous and has been extensively tested by comparison with experiment. Because the flat slabs and flat wedge wells lack circumferential curvature, polarization effects are separate for transverse electric (TE) and transverse magnetic (TM) waves.

In 1980 and 1981, we analyzed fields near a finite slab, length 10 inch and thickness 1/8 inch for wavelength 1.259 inch (Reference 5). The total and scattered fields were computed by the moment method for grazing incidence but only for perpendicular polarization. The main result was a resolution of the field distribution into constituent fields, which were the incident wave, edge-scattered cylindrical waves, a guided wave propagating in the direction of the incident wave, and a guided wave propagating backward toward the source.

However, practical radomes usually resemble axially symmetric shells more closely then wedges. Therefore, we also investigated the fields near an axially symmetric shell. The purpose in investigating an axially symmetric shell was to determine whether the fields can be decomposed into simple, constituent waves that resemble those on slabs and wedges. This decomposition is analogous to solving canonical problems in the geometric theory of diffraction.

3.1 HOMOGENEOUS DIELECTRIC SLAB, LENGTH 3.18 WAVELENGTHS

The moment method was utilized to compute the fields near a slab with the parameters given in Table 3.1-1. Slab coordinates are defined in Figure 3.1-1. Incidence was grazing, and the wavelength used was 1.259 inch. Calculations were done for both parallel and perpendicular polarizations, which correspond respectively to transverse magnetic (TM) and transverse electric (TE) fields. The slab was divided into 33 cells.

Table 3.1-1. Parameters of Homogeneous Slab

Length:	4 in.
Thickness:	0.125 in.
Dielectric constant:	2.6 in.

The magnitude of the total field at the cell centers is shown in Figure 3.1-2 for parallel and perpendicular polarizations. E^T is larger for perpendicular polarization. The rapid oscillations for perpendicular polarization can be explained by interference between guided waves propagating in opposite directions.
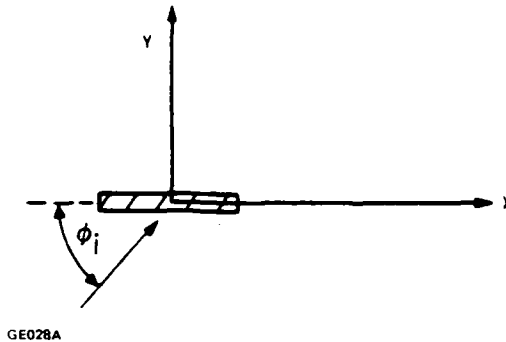
Figure 3.1-1. Coordinates for a Slab

The phase values of E^T are shown in Figure 3.1-3. The phase increment with position is obtained from the propagation constants k_g of waves guided by an infinitely broad slab. Transcendental equations are solved which have the following form for even TE modes (Reference 8):

$$- (ua/2) \cot(ua/2) = (va/2) \tag{3-1}$$

$$u^2 + v^2 = k_o^2(\kappa - 1) \tag{3-2}$$

where a is slab thickness, k_o is $2\pi/\lambda$, λ is the wavelength, and κ is dielectric constant. For odd TM modes Equation (3-1) is replaced by

$$(ua/2) \tan(ua/2) = (va/2) \tag{3-3}$$

The propagation constants for the slab of Table 3.1-1 are given in Table 3.1-2.

Table 3.1-2. Guided Wave Propagation Constants for Slab of Table 3.1-1

Mode	k_z
Lowest even TE	1.758 π/inch
Lowest even TM	1.634 π/inch

For the TE mode, k_z gives phase delay 316°/inch, compared to the moment method results of 308°/inch (Figure 3.1-3). For the TM mode, k_z gives 294°/inch, compared to the moment method which gives 290°/inch. This close agreement supports the interpretation of slab-guided modes even in the short slab of length 3.18 wavelength. The difference between the phase delay for perpendicular and parallel polarizations will be shown to be significant for axially symmetric radomes.

Figure 3.1-2. Total Field Magnitude Inside 4-Inch Long, 0.125-Inch Thick Slab;
Dielectric Constant 2.6; Frequency 9.40 GHz; Grazing Incidence

Figure 3.1-3. Phase for Figure 3.1-2 (+); Incident Field Phase (•)

The distribution of the total field E^T near the slab is shown in Figure 3.1-4, and the scattered field $E^T - E^I$ is shown in Figure 3.1-5. These results are fo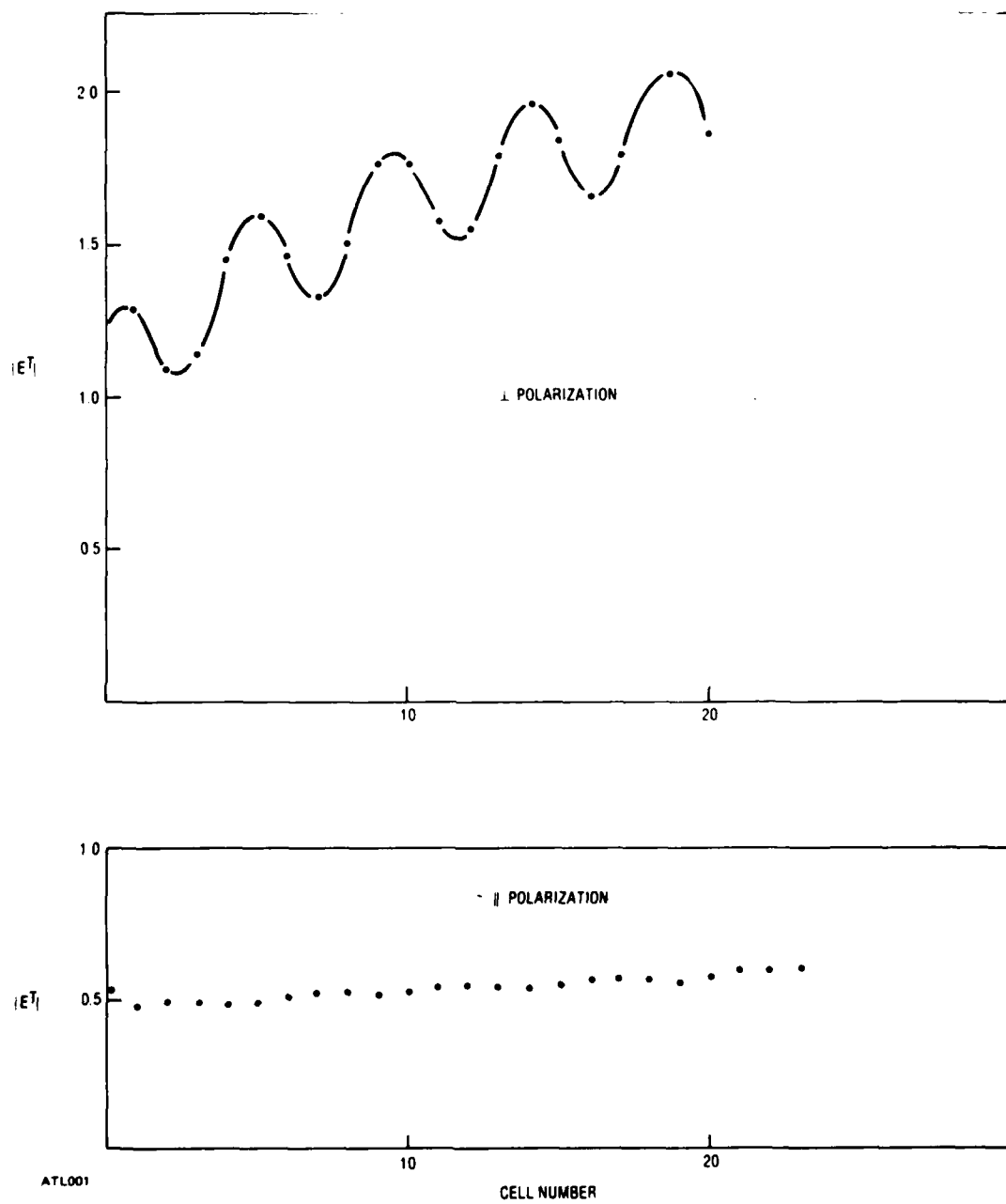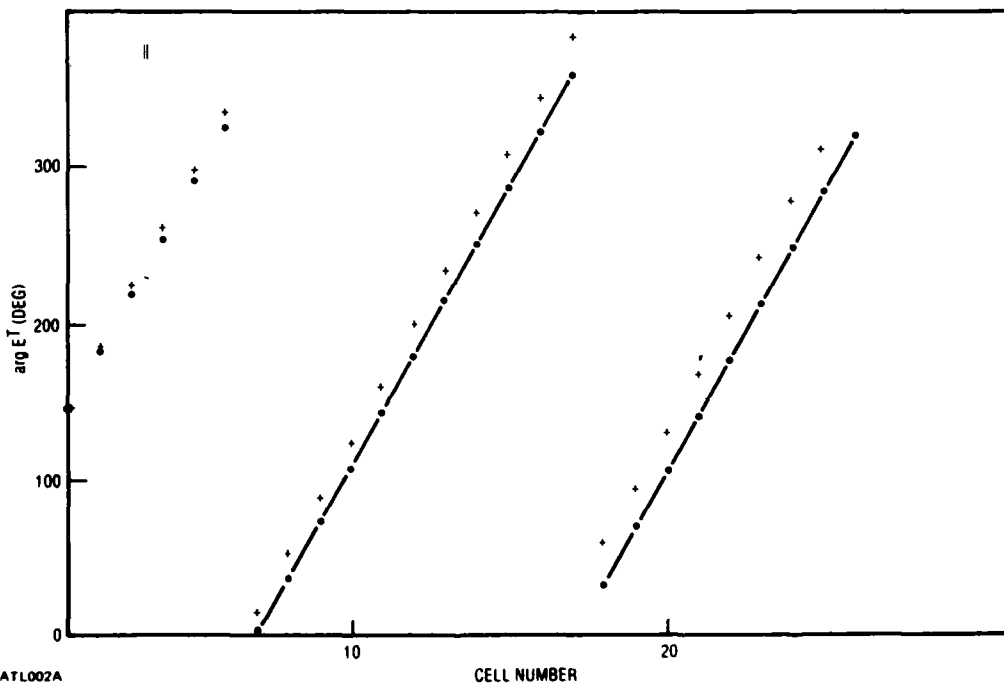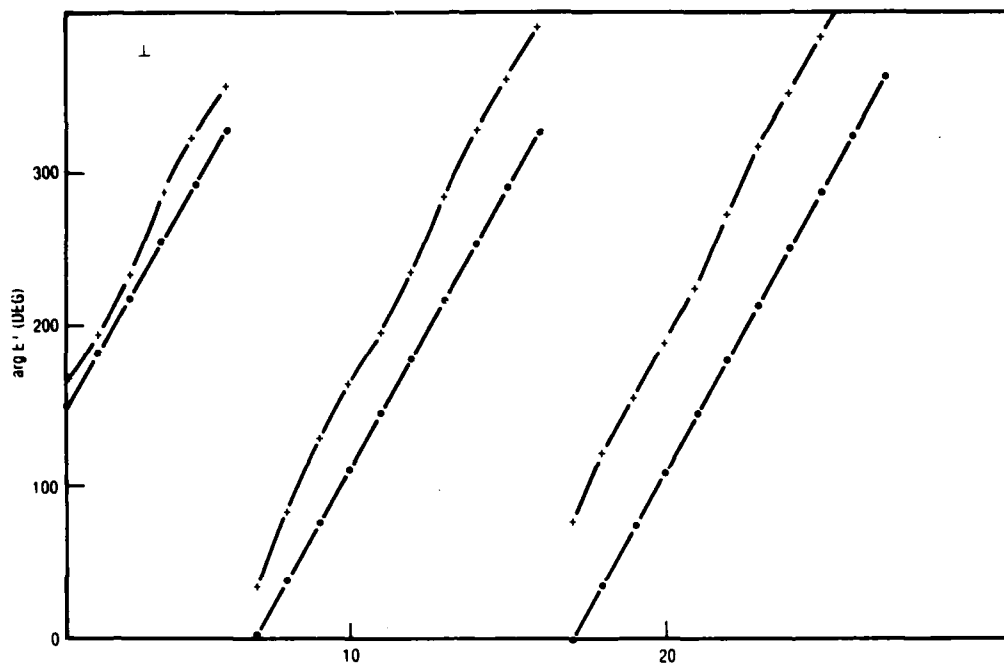r the value $X = D$, the plane midway through the slab length. Notice that for parallel polarization a component of field is found in the x direction, although the incident field has no x component.

The scattered field E^S computed by the moment method has an exponential decrease outside the slab region. For a TE mode, a slab-guided wave decreases as $\exp(-v)\,|y - \frac{a}{2}|$), where $v = 0.704\pi/\text{inch}$. For a TM mode, a guided wave decreases with $v = 0.336\pi/\text{inch}$. The exponential decreases are graphed in Figure 3.1-6, with the assumptions that exponential decrease starts at $y = 0.1$ inch and that the field magnitudes are assumed correct at that value of y.

The minima in $|E^T|$ occur at $Y = 0.6$ in. for the TE case and $Y = 1.0$ in. for the TM case (Figure 3.1-4). These locations correspond to phase values of π in E^S, as seen in Figure 3.1-5, and the zero value of phase of E^I.

We conclude that guided waves exist and produce effects at distances as large as one wavelength from the slab. These distances are an appreciable part of the diameter of small missile radomes.

In Figure 3.1-4, the phase of E^T varies with Y more rapidly for the TE wave (or perpendicular polarization) than for the TM wave (parallel polarization). This result is significant for radomes and possibly for guided wave integrated antennas.

3.2   TWO-LAYER SLAB, LENGTH 3.18 WAVELENGTHS

Because the calculations for the homogeneous slab showed appreciable guided wave magnitude, additional calculations were done for a thicker slab. This slab consisted of two layers: one layer was identical to that of the homogeneous slab in the preceding section (Table 3.1-1); the second layer had the same thickness, but a different dielectric constant. The parameters are listed in Table 3.2-1. The slab was analyzed to evaluate how a second layer affects guided wave excitation and decrease with distance from the slab. The wavelength used was 1.259 in.

Table 3.2-1. Parameters of Two-Layer Slab

Length:	4 in.	
Thickness:	layer 1	0.125 in.
	layer 2	0.125 in.
Dielectric Constant:	layer 1	2.6
	layer 2	4.0

Figure 3.2-1 shows $|E^T|$ for $x = 0$, the plane dividing the slab symmetrically. By comparing Figures 3.2-1 and 3.1-4 for parallel polarization, we see larger maximum values of $|E^T|$ for the thicker slab. In contrast, for perpendicular polarization the maximum value of $|ET|$ is smaller for the thicker slab.

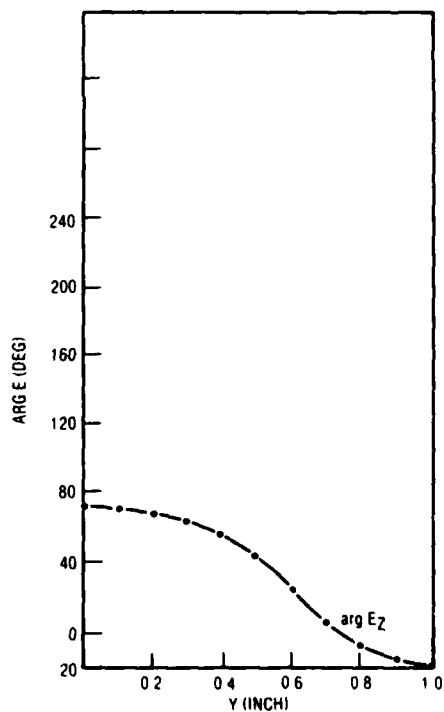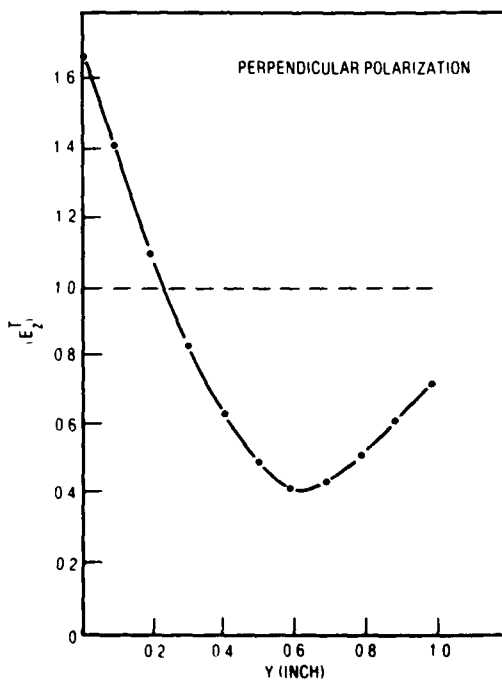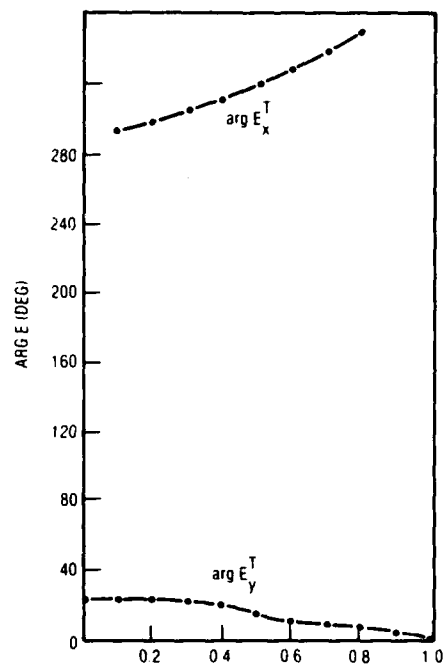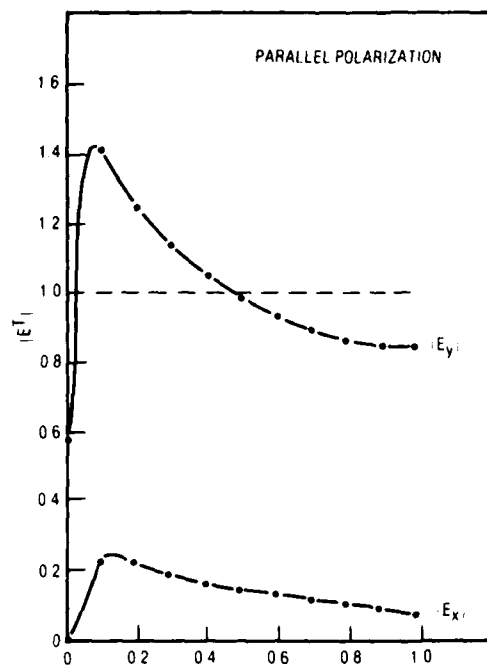Figure 3.1-4. Total Field on Transverse Plane X = 0, for 4-Inch Long Slab;
Thickness 0.125-in.; Grazing Incidence Cell Radii 0.0715-in.;
Frequency 9.4 GHz; Dielectric Constant 2.6

3-6
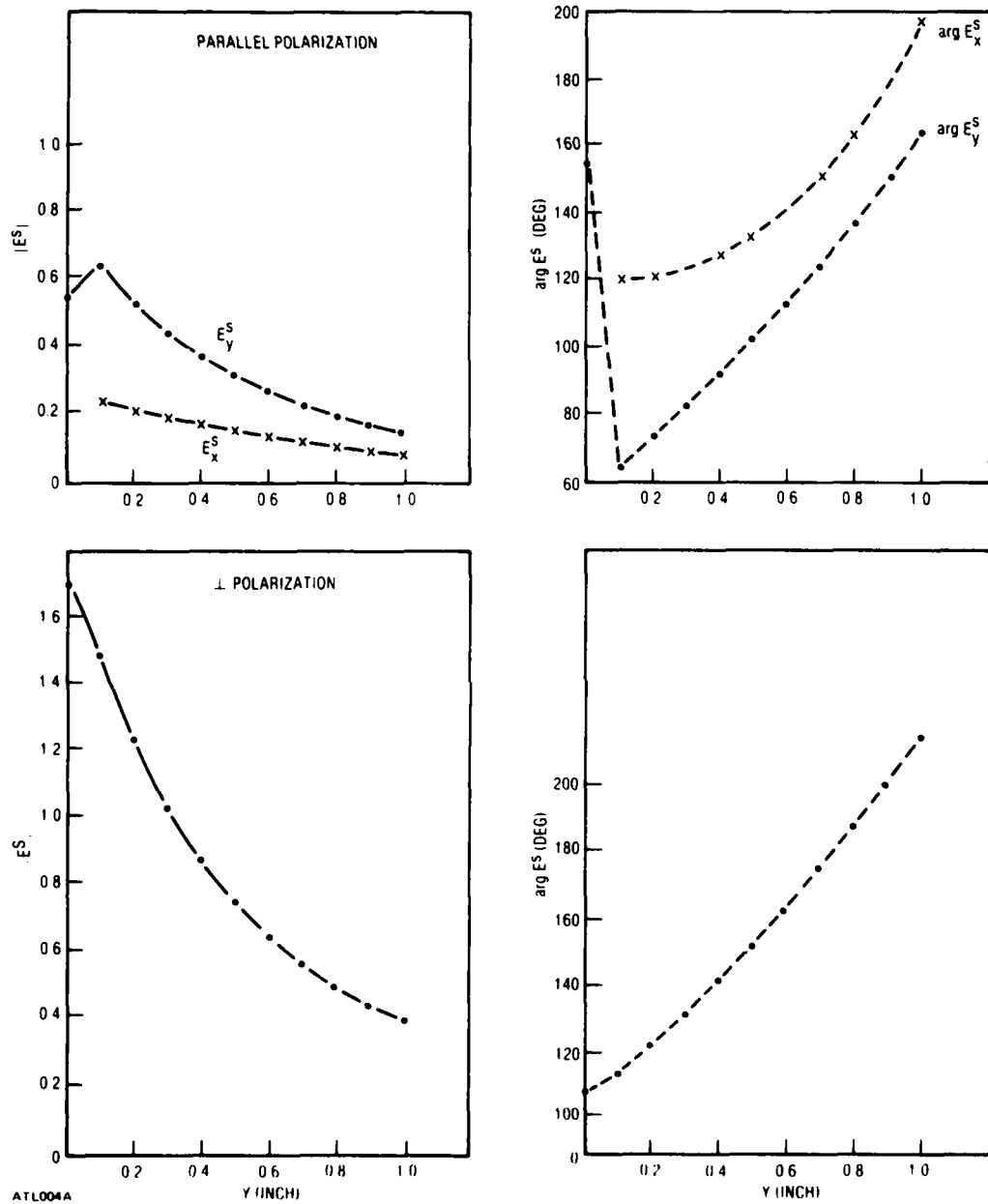
Figure 3.1-5. Scattered Field for Figure 3.1-4
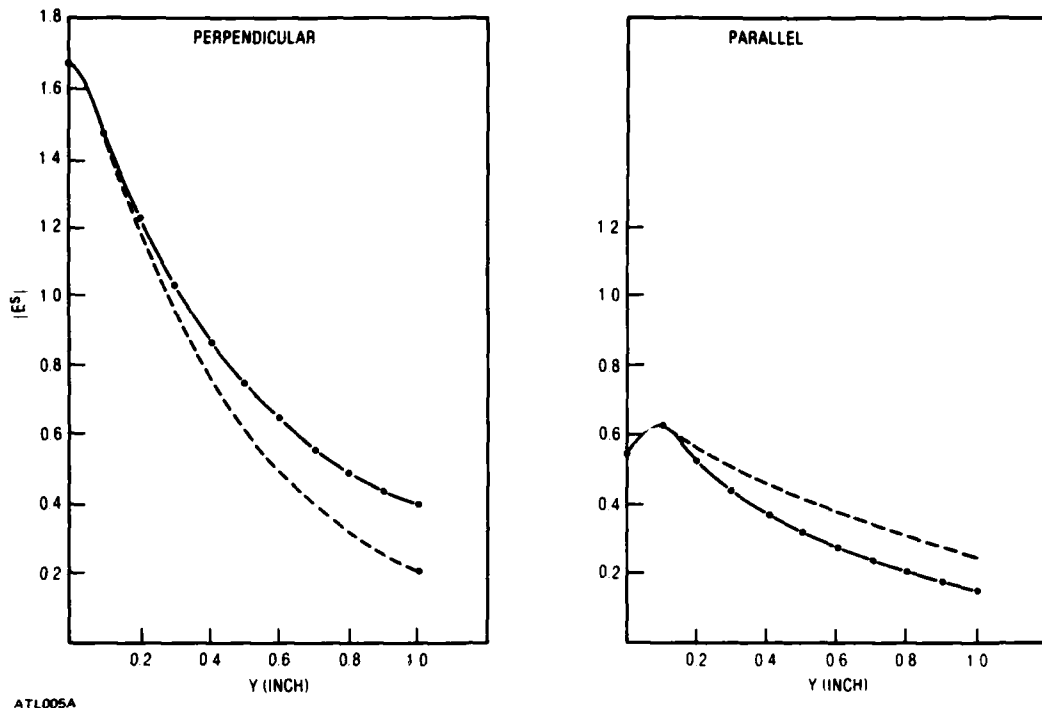
Figure 3.1-6. Magnitude of Scattered Field; by Moment Method (•);
by exp (-v |y -0.1|)-

The phase of E^T is shown in Figure 3.2-2. The changes of phase with Y have opposite signs for the two polarizations. If the slab is taken to be a model of one side of an axially symmetric radome with grazing incidence on that side, then the difference in the signs of the spatial derivative of phase implies opposite signs of boresight error.

Figure 3.2-3 shows $|E^S|$, and Figure 3.2-4 shows arg E^S. Significant differences exist for the two polarizations.

3.3 HOLLOW WEDGE WITH WALLS OF LENGTH 3.18 WAVELENGTHS

As a step toward analyzing axially symmetric structures, moment-method calculations were done for a hollow wedge consisting of two slabs like those in Section 3.2. The parameters of the wedge are listed in Table 3.3-1, and its dimensions are shown in the coordinate system of Figure 3.3-1. The wavelength used was 1.259 in.

The total field magnitude $|E^T|$ inside the wedge is shown in Figure 3.3-2 for perpendicular polarization and in Figure 3.3-3 for parallel polarization. The figures also show $|E^T|$ for grazing incidence on a single slab. The values of $|E^T|$ for grazing incidence on a slab are very close to those for the wedge's lower wall, which is also illuminated at grazing incidence.

PARALLEL

$|E_y^T|$

$|E_y|$

PERPENDICULAR

$|E_z^T|$

Y (INCH)

ATL006
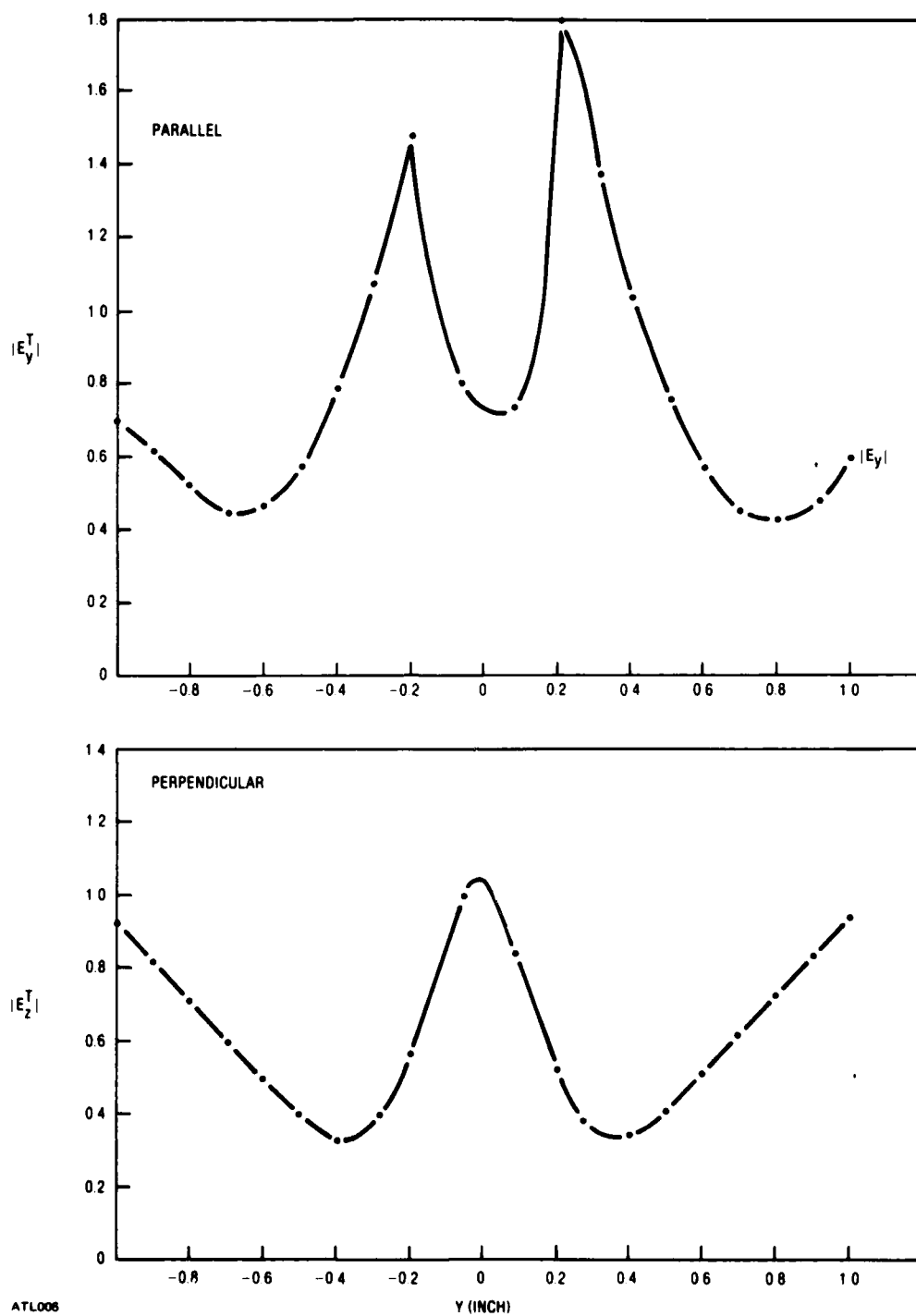
Figure 3.2-1. Total Field for Two-Layer Slab, Grazing Incidence, on Plane x = 0
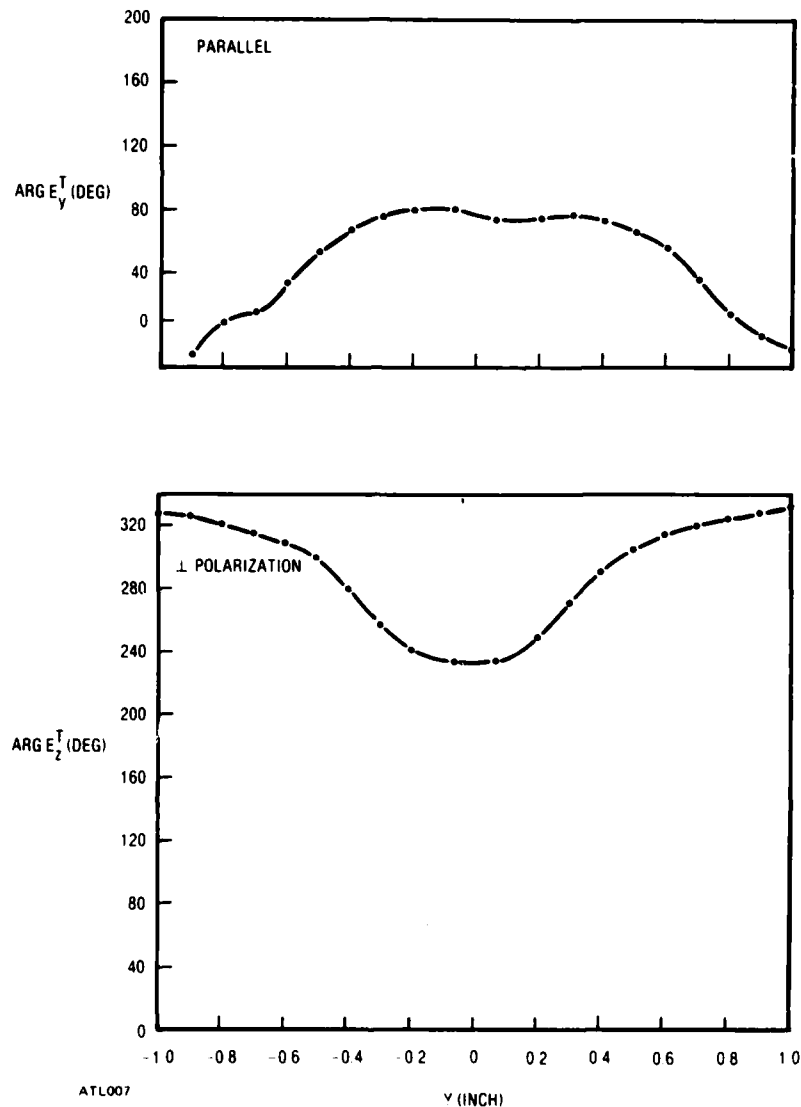
Figure 3.2-2. Phase of E^T Corresponding to Figure 3.2-1

For axial incidence, Figure 3.3-4 shows the z component of the total field E_z^T in the symmetric transverse plane (x = 2 in.) for perpendicular polarization. Figure 3.3-5 shows E_y^T for parallel polarization. Notice that $|E_x^T|$ is not zero; this is becuase the wedge generates a field component in the direction of propagation of the incident wave.

The phase curves in Figures 3.3-4 and 3.3-5 are different for the two polarizations. In addition, the phase values depend on the direction of the incident wave. The dependence on incidence direction results in boresight error, and differences in the phase curves mean that boresight error depends on polarization.

3-10
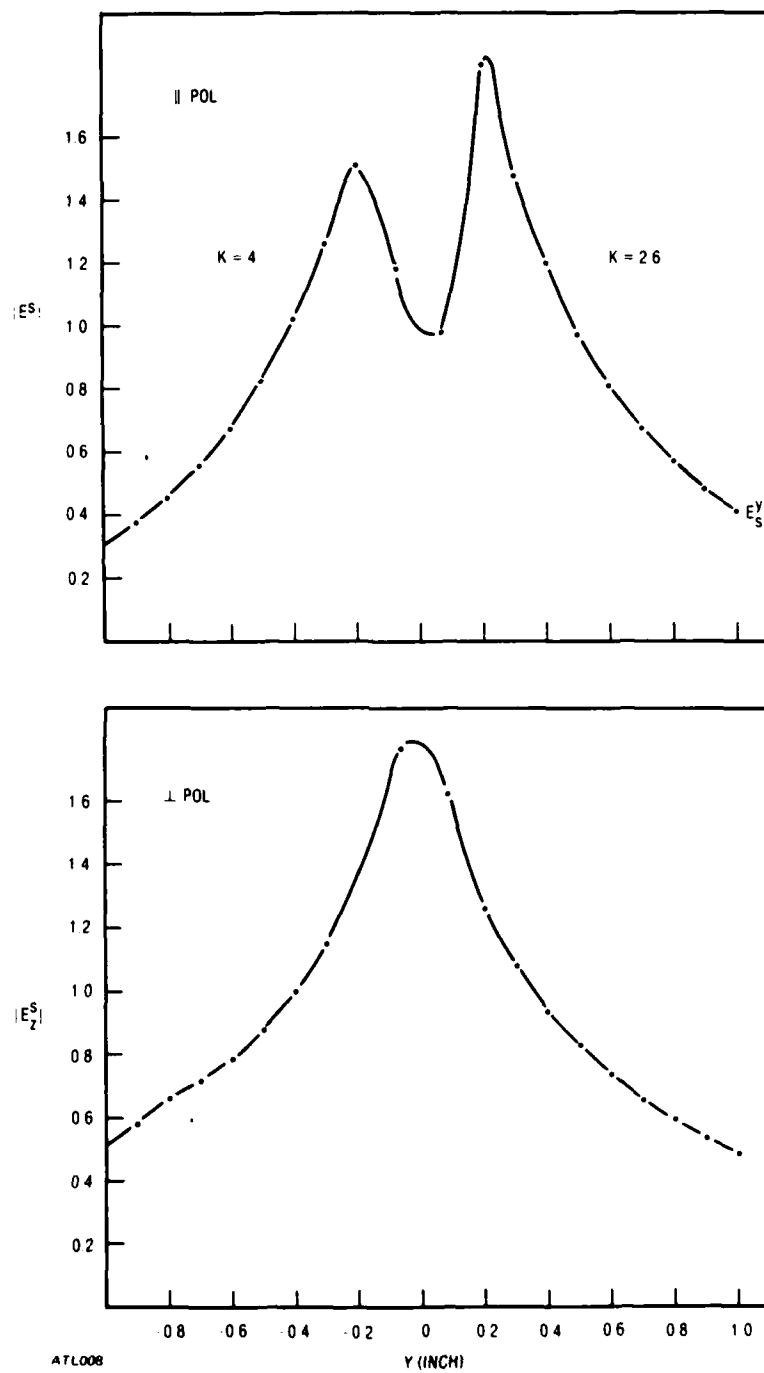
Figure 3.2-3. Scattered Field for Figure 3.2-1

3-11
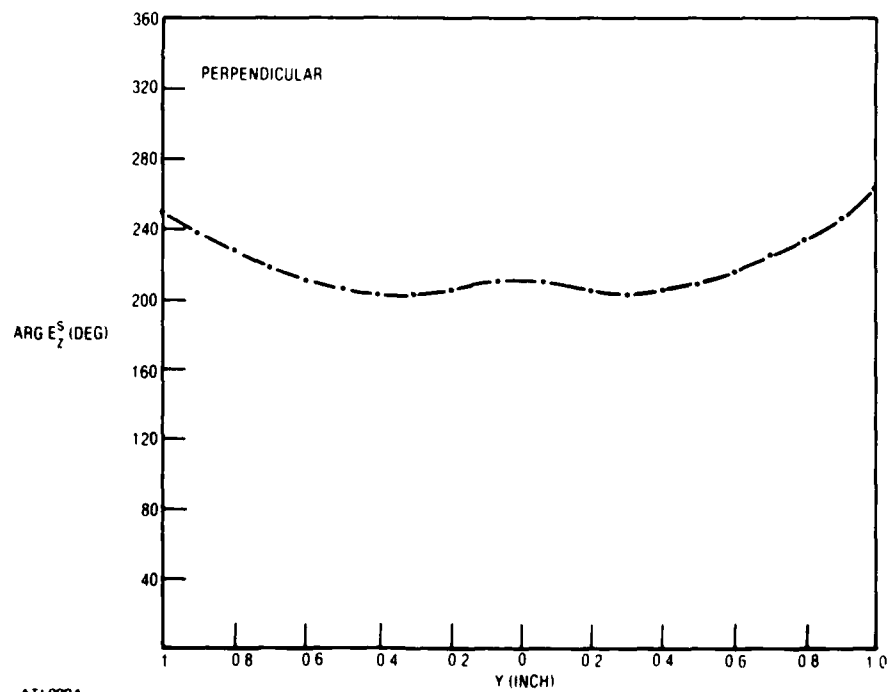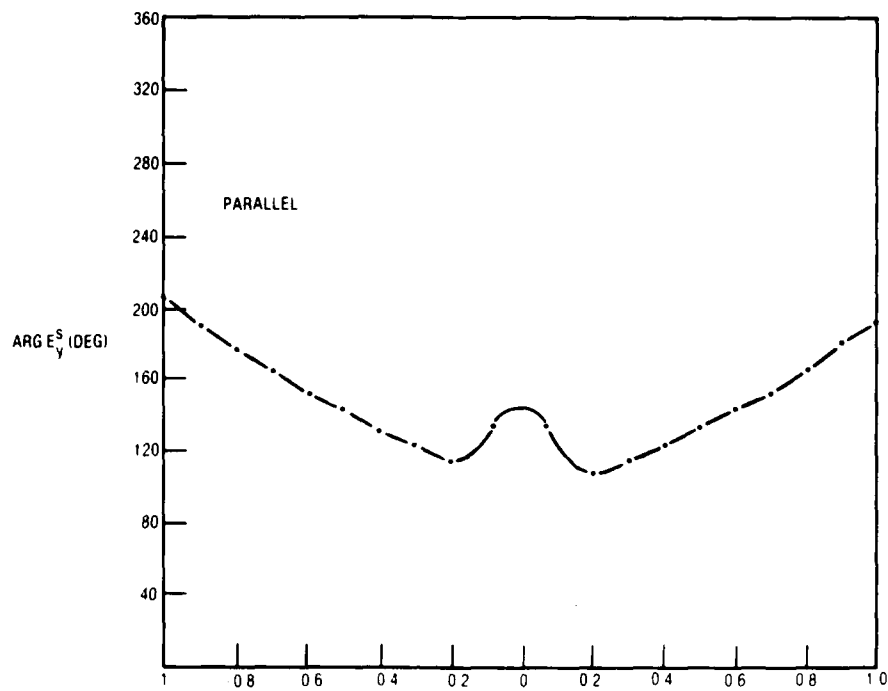
Figure 3.2-4. Phase for Figure 3.2-3

Table 3.3-1. Parameters of Wedge

Length of Sides	4 in.
Thickness of Walls	0.125 in.
Half Angle	16.5
Dielectric Constant:	2.6

To quantify these effects on boresight error we measured the phase-delay difference between two points symmetrically located about the wedge axis with their centers 2.25 in. (1.8 wavelength) from the wedge vertex. Figure 3.3-6 shows the phase differences between the pairs of points. Notice that the differences for perpendicular polarization have larger magnitudes than those for parallel polarization. This result is significant for electronic compensation for it implies the need for polarization sensing.

In the calculations for parallel polarization, the rectangular components E_x and E_y were projected onto the baseline to simulate an aperture antenna.

ATL010
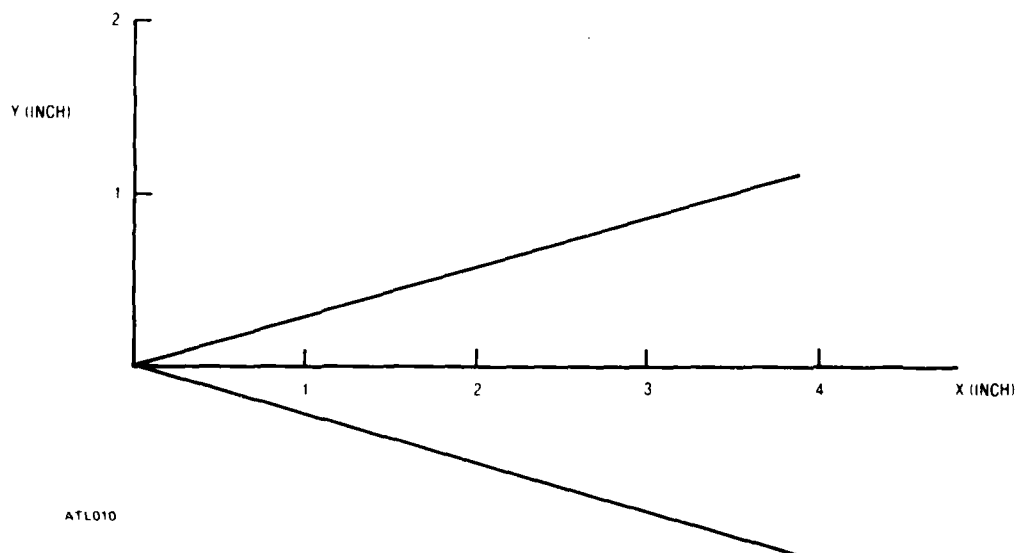
Figure 3.3-1. Coordinates for Wedge

3.4 AXIALLY SYMMETRIC SHELL

The shell's outer contour is shown in Figure 3.4-1. It is a curve with radius

$$r = R(x - L)^{1/2}$$

where R is the base radius and x is the axial coordinate. The radome was fabricated from a resin, with dielectric constant 2.1, and its thickness tapers from 0.175 in. at the tip to 0.130 in. at the base.

3-13
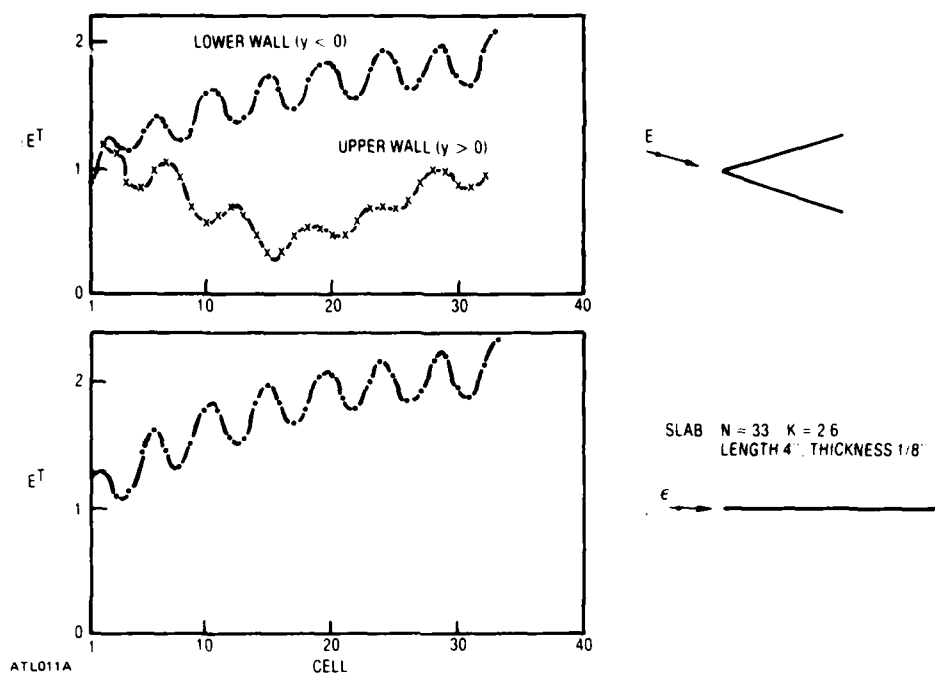
Figure 3.3-2. Total Field; Perpendicular Polarization, Inside Wedge, for
Grazing Incidence on Lower Wall, and Total Field Inside Slab.
Number of cells: wedge, 65; slab, 33
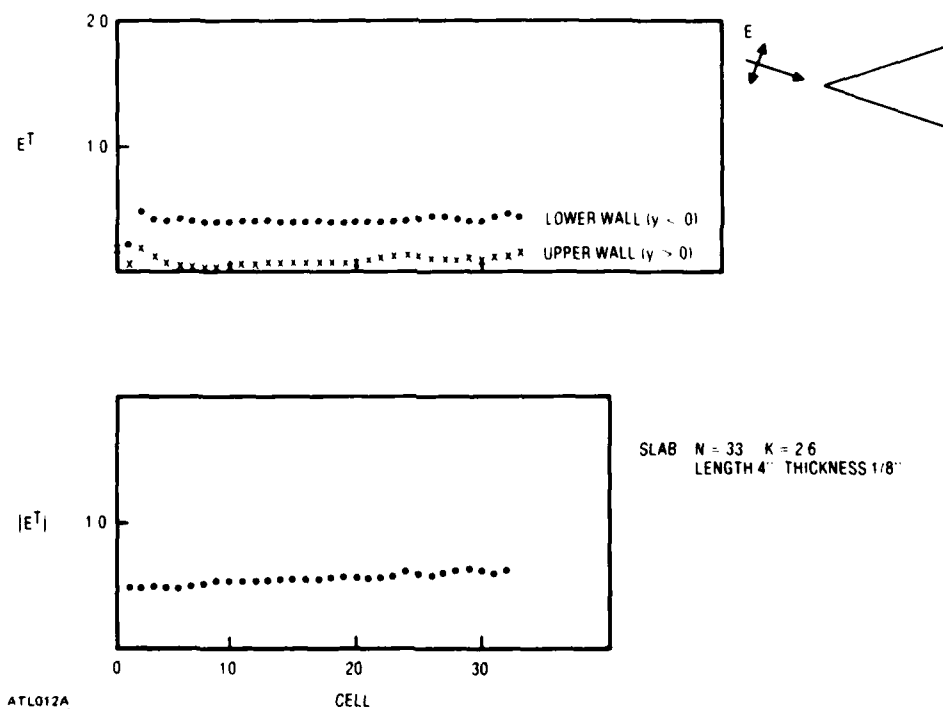
Figure 3.3-3. As in Figure 3.3-2, but for Parallel Polarization

3-14
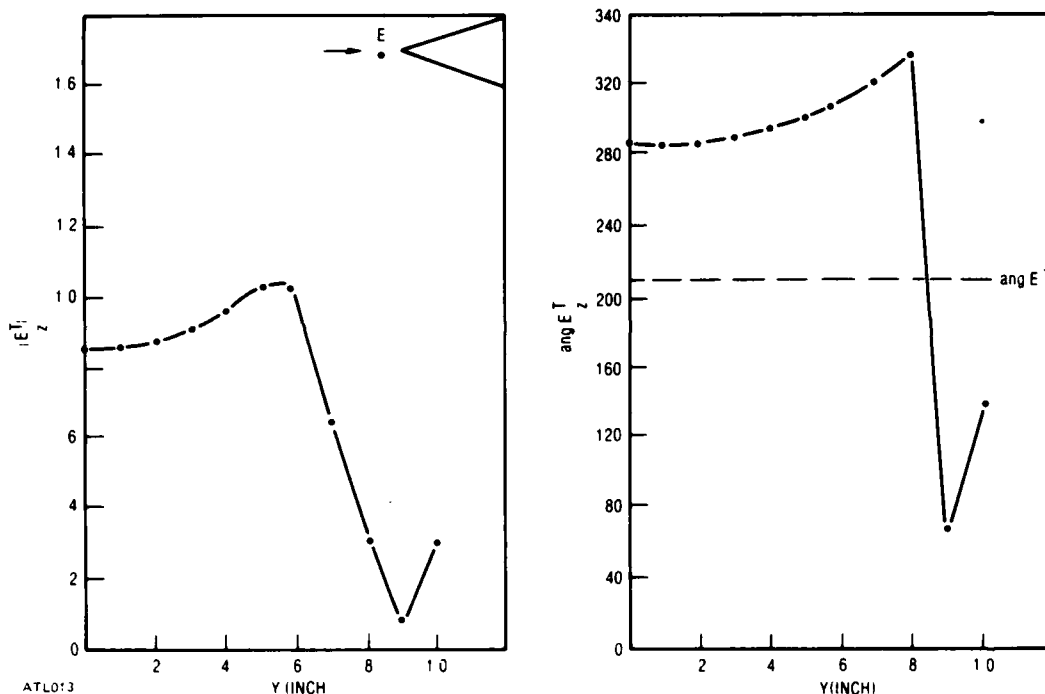
Figure 3.3-4. Total Field at x = 2-in. for Wedge, Axial Incidence,
Perpendicular Polarization

3.4.1 WAVEFRONT MEASUREMENTS

The phase and intensity in side the shell were measured by scanning a small probe antenna (aperture 1.25-in. square) over a linear path with approximately plane waves incident externally. The receiver was a network analyzer, and a waveguide path propagated the coherent reference field. The radome was supported by an absorber-covered frame that provided rotation about a vertical axis to vary the incidence direction defined in Figure 3.4-2 by the gimbal angle β, which is between the incident wave normal and the radome axis. The radome was pivoted about a point on the radome axis 1.5 in. from the base, and the probe aperture scanned a horizontal line 1.5 in. closer to the tip. The frequency used was 10.000 GHz (wavelength = 1.180 in.).

Measured power transmittance and phase delay are shown in Figures 3.4-2 and 3.4-3 for horizontal polarization; this scan direction and polarization are the E-plane. Figures 3.4-4 and 3.4-5 show transmittance and phase delay for vertical polarization; this case is referred to as the H-plane.

Figure 3.4-2 shows very low transmittance values for horizontal displacements near 2 in. The phase delay curves in Figure 3.4-3 have overall slopes that change from positive to negative as β is changed. This change in slope implies a change in the sign of boresight error with gimbal angle and a zero value at approximately 6°. In contrast, for vertical polarization the slope is negative for most gimbal angles although for larger angles, like 16°, the phase tilt is becoming positive.

3-15
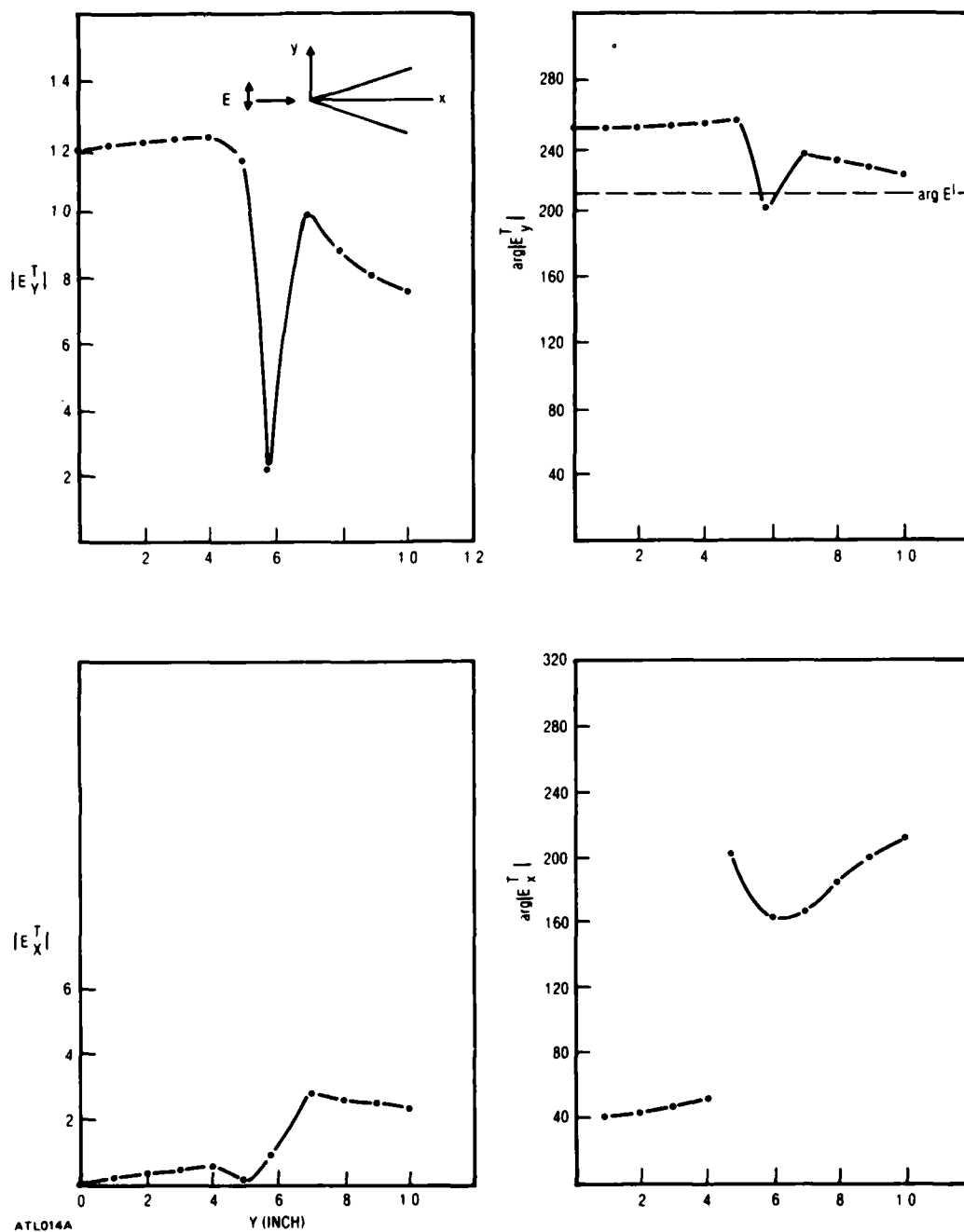
Figure 3.3-5. As in Figure 3.3-4, but for Parallel Polarization
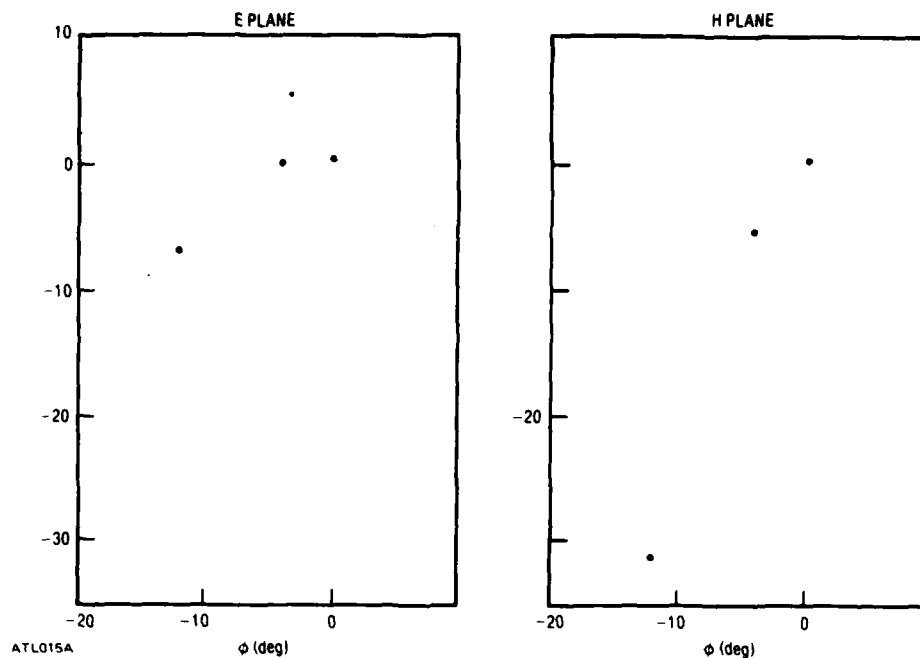
Figure 3.3-6. Phase Difference Between Two Points;
Separated by 0.9 in. at x = 2.25 in. within Wedge

The low transmittance values near the wall for the E-plane are surprising because, for flat sheets, parallel polarization has high transmittance. The low values suggest guided waves, as do the values that exceed 0 dB.

3.4.2 BORESIGHT ERROR MEASUREMENTS

Boresight error was estimated by measuring the phase difference between a pair of horn antennas. The antennas were connected to a network analyzer. Each horn had E-plane aperture 1.7 in. and H-plane aperture 2.1 in. The antennas were spaced by 2.1 in. in the H-plane. Measurements were made by pivoting the radome and recording phase difference. The antennas were used in two angular orientations, rotated about the symmetry axis of the pair, to measure E- and H-plane errors; incident wave polarization also was rotated.

Figures 3.4-6 and 3.4-7 show measured phase differences. Note the sign reversal in the E-plane data near ±6° gimbal angle. That is, the phase differences for β less than 6° have signs opposite to those for β exceeding 6°. This sign reversal does not occur for the H-plane (Figure 3.4-7). The sign reversal in the E-plane and its absence in the H-plane are reasonable when we consider the probing data (see the discussion in subsection 3.4.1). Moreover this behavior is suggested by the moment-method results in Figure 3.3-6.

3-17
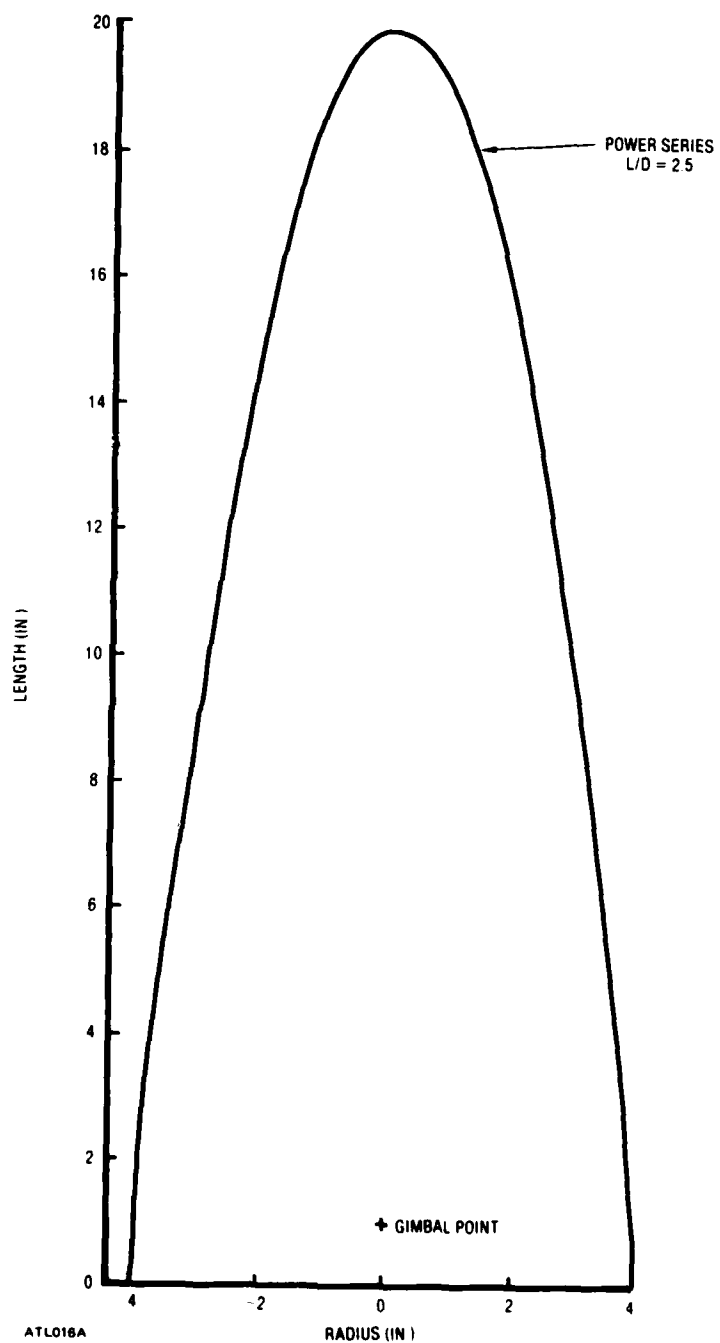
Figure 3.4-1. Contour of Axially Symmetric Shell

3-18
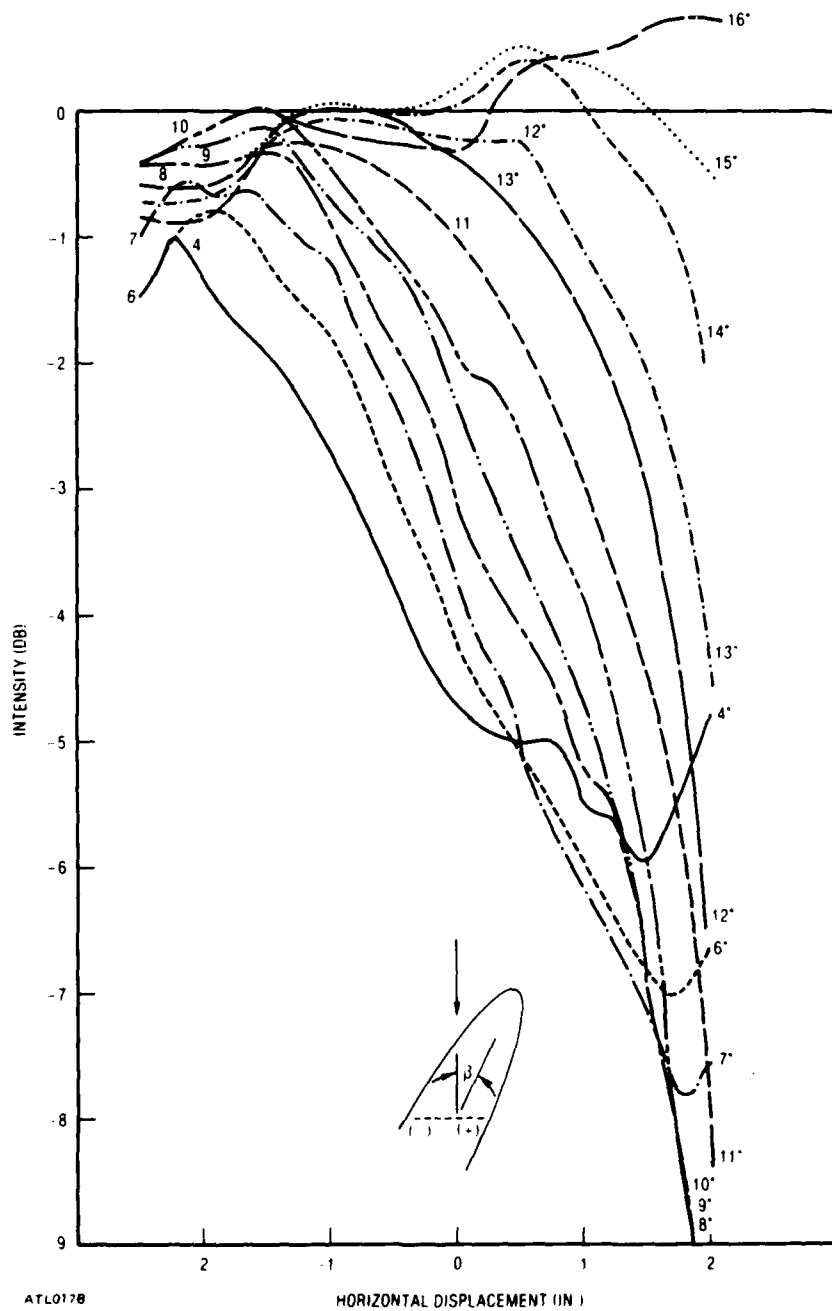
Figure 3.4-2. Intensity Transmittance of Axially Symmetric Shell.
The inset shows the probing path as a dotted line; the graphs
are labeled with values of β, horizontal polarization

3-19

STYCAST L/D = 2 5
MEAS 2-17-82 1 25 × 1 25 HORN
E-PLANE (H-POL) 10 GHZ
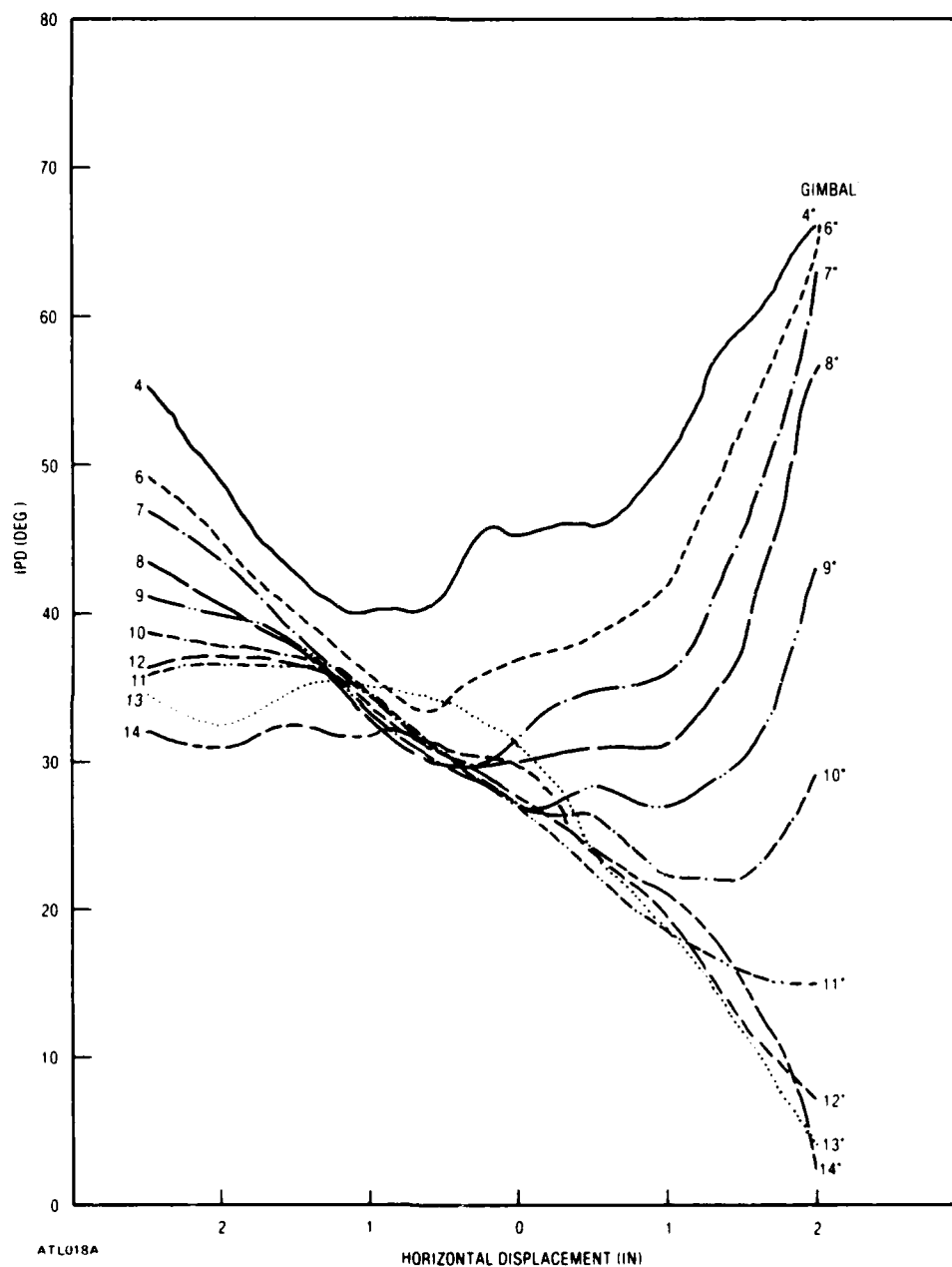
Figure 3.4-3. Phase Delay (IPD) of Axially Symmetric Shell for
Horizontal Polarization

3-20
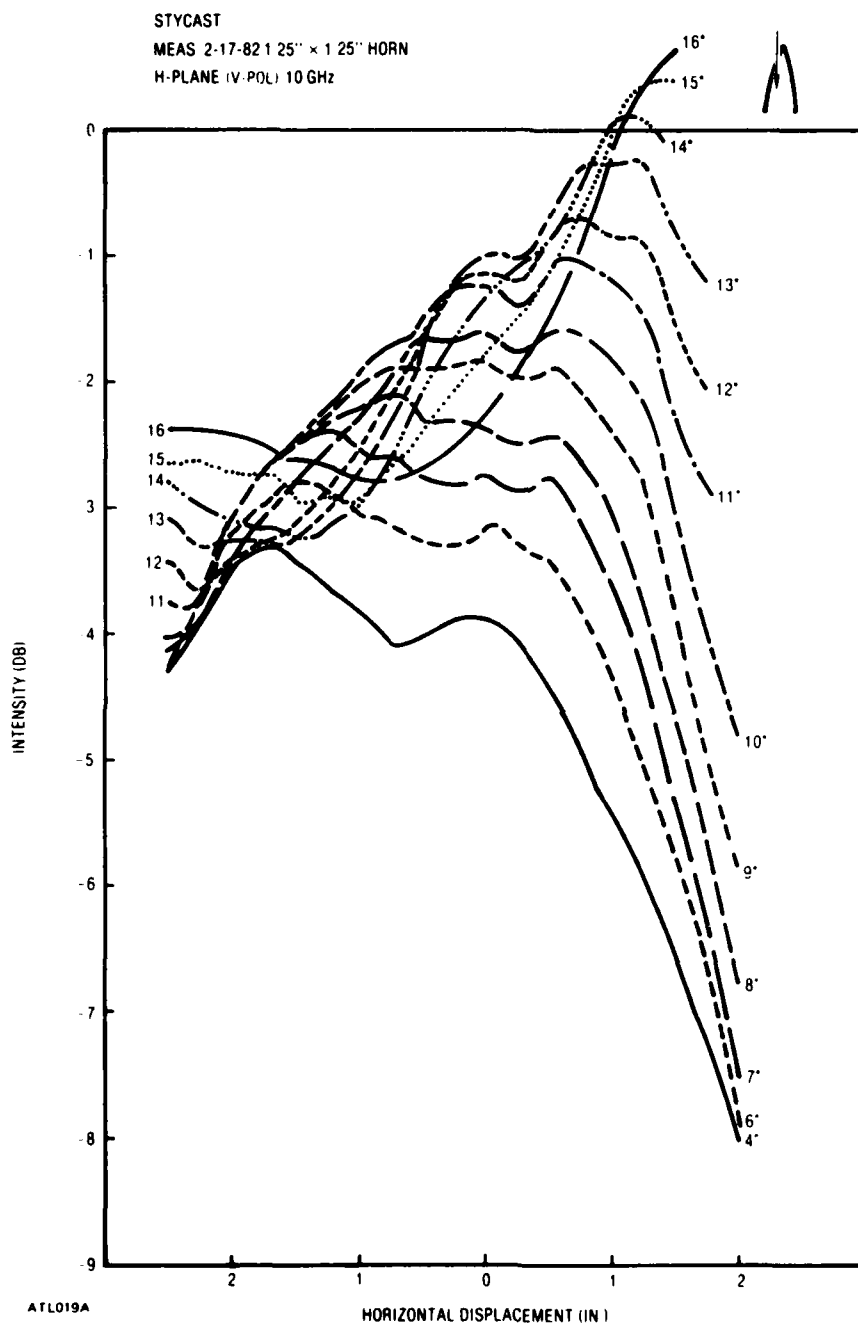
Figure 3.4-4. Intensity Transmittance of Axially Symmetric Shell,
Vertical Polarization

3-21

STYCAST L/D = 2.5
MEAS 2-17-82 1 25" × 1 25" HORN
H-PLANE (V-POL) 10 GHz
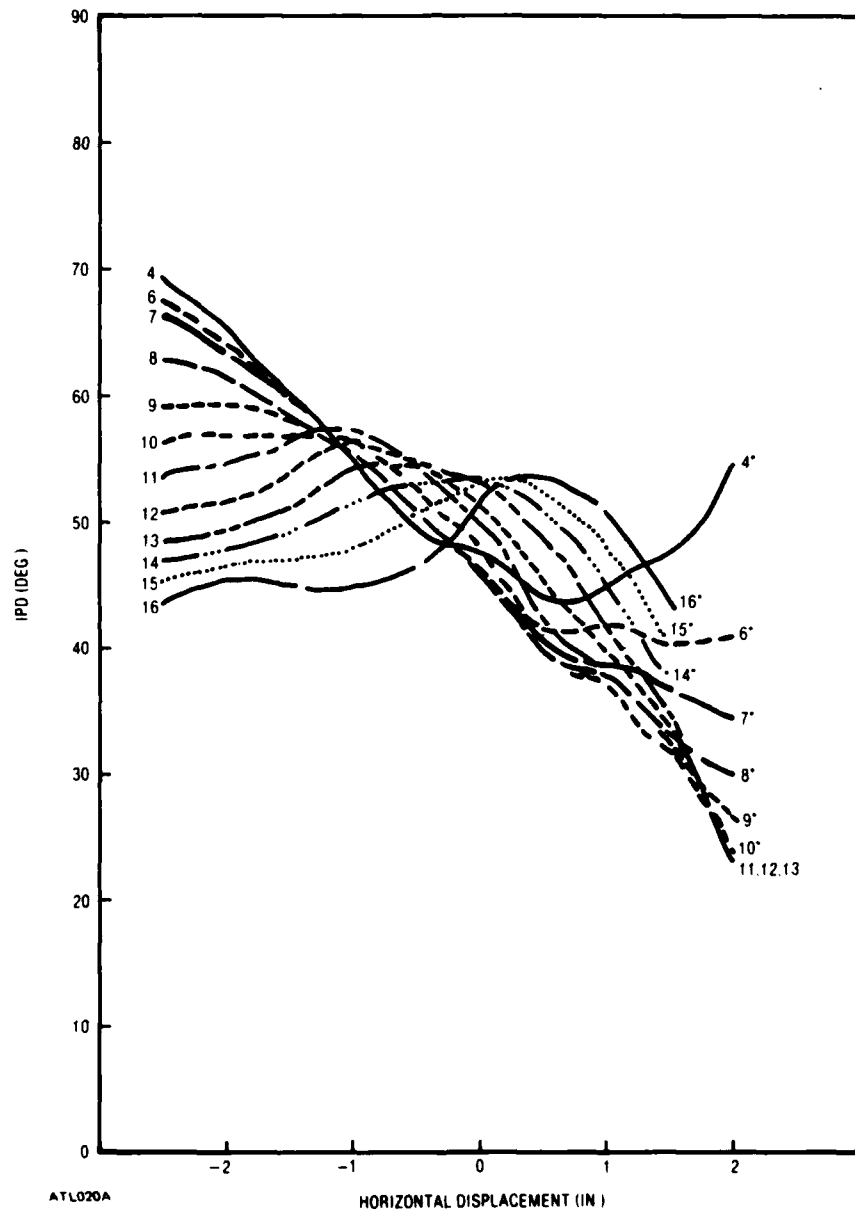
Figure 3.4-5. Phase Delay (IPD) for Shell, Vertical Polarization

3-22
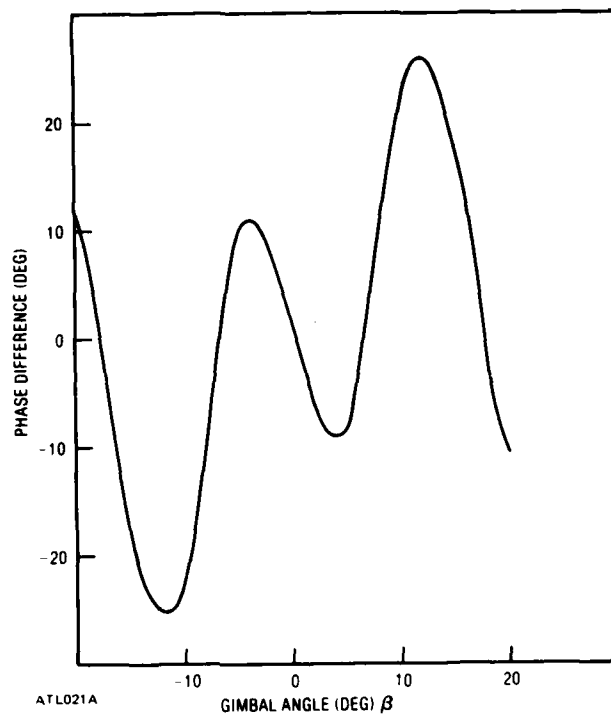
Figure 3.4-6. E-Plane Phase Difference Between Two Antennas; Frequency 10 GHz
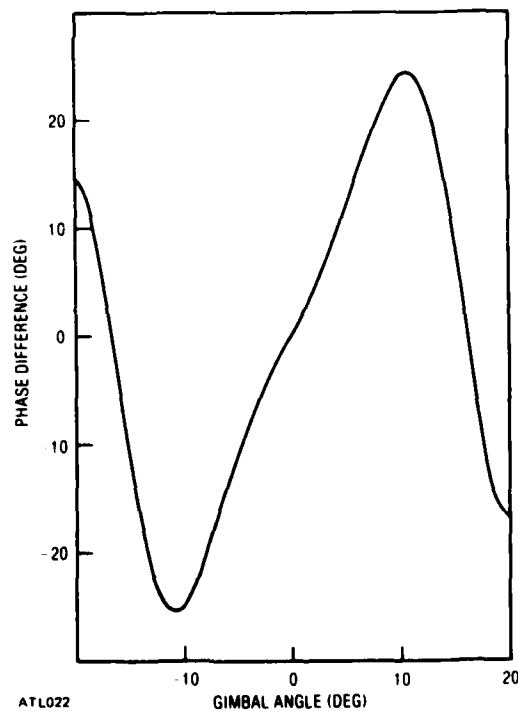
Figure 3.4-7. H-Plane Phase Difference Between Two Horn Antennas;
Frequency 10 GHz

3.4.3 WAVEFRONT ANALYSIS

This section describes the analysis of the measured wavefronts into two separate fields. The procedure starts with the computation of the wavefront field E_c by means of the surface integration method (Figure 2-2). The second step is to subtract E_c from the measured values E_m. The difference $E_m - E_c$ is then analyzed to determine its properties.

The details of computing E_c are as follows. The integration is confined to an area defined by the first Fresnel zone which is defined by the transverse radius $r = \sqrt{\lambda \ell}$ where λ is wavelength and ℓ is the distance from the observation point (on the probing surface) to the incident wavefront surface containing the Fresnel zone. The validity of using the first Fresnel zone has been discussed in another report (Reference 7). The integration mesh size is not very critical so long as the spacing of convergent rays, in the Fresnel zone, is approximately a half-wavelength. The value of ℓ is a critical parameter because it influences sampling, therefore E_c was calculated for ℓ equal to 10, 20, 30, 40, and 50 wavelengths. The computed values of E_c were compared with E_m, and those for ℓ equal 40λ agreed most closely with the measured. This value of ℓ gives an illuminated area on the radome that agrees rather well with that found earlier for a shorter radome that had the same base diameter as the shell, but was only 16.5 in. long.

Figure 3.4-8 shows samples of intensity ($|E_c|^2$ or $|E_m|^2$) and phase (E_c or E_m). The discrepancies in phase delay are largest for Y_A (the transverse coordinate in the probing path), approximately equal to 2 in. The region in which the probe approaches the wall that is illuminated at approximately grazing incidence, is shown in the inset. The radome offset (gimbal) angle β was 15°. The discrepancies of phase in Figure 3.4-8 imply significant discrepancies in boresight error calculations that omit guided waves.

The difference between E_m and E_c was calculated and $|E_m - E_c|$ and arg $(E_m - E_c)$ plotted for β equal 15° (Figure 3.4-9). Also plotted are two curves that describe the exponential decrease of field magnitude for a slab-guided wave. Specifically, the graphs show $0.26 \exp(-v|y-2|)$ where 0.26 is the value computed for $|E_m - E_c|$. The two exponential curves are for v equal 0.75/inch and 1.01/inch; these values were calculated for infinite slabs with thicknesses 0.125 in. and 0.150, respectively.

The agreement between $|E_m - E_c|$ and the exponential curves supports the view that the radome causes guided waves, and that these guided waves are of the relatively simple type that propagate on slabs. The magnitude of the guided wave is appreciable, but of more importance is the phase.

The phase variation of $E_m - E_c$ (Figure 3.4-9) can also be explained in terms of slab-guided waves. If we assume a slab-guided wave, the equiphase surface in Figure 3.4-10 describes the phase surface. This phase surface crosses the probing path at angle of approximately 10°, not 15°, because the radome has axial curvature. The phase variation caused by the assumed guided wave is then ($k_g \, \Delta y_A \sin \theta$), where θ is the angle between the wavefront and the probing path, y_A is displacement, and k_g is the propagation constant of the slab-guided wave. For thickness = 0.125 in., k_g is 1.720π/inch, and for thickness = 0.150 in., k_g is 1.751π/inch. A graph of phase change

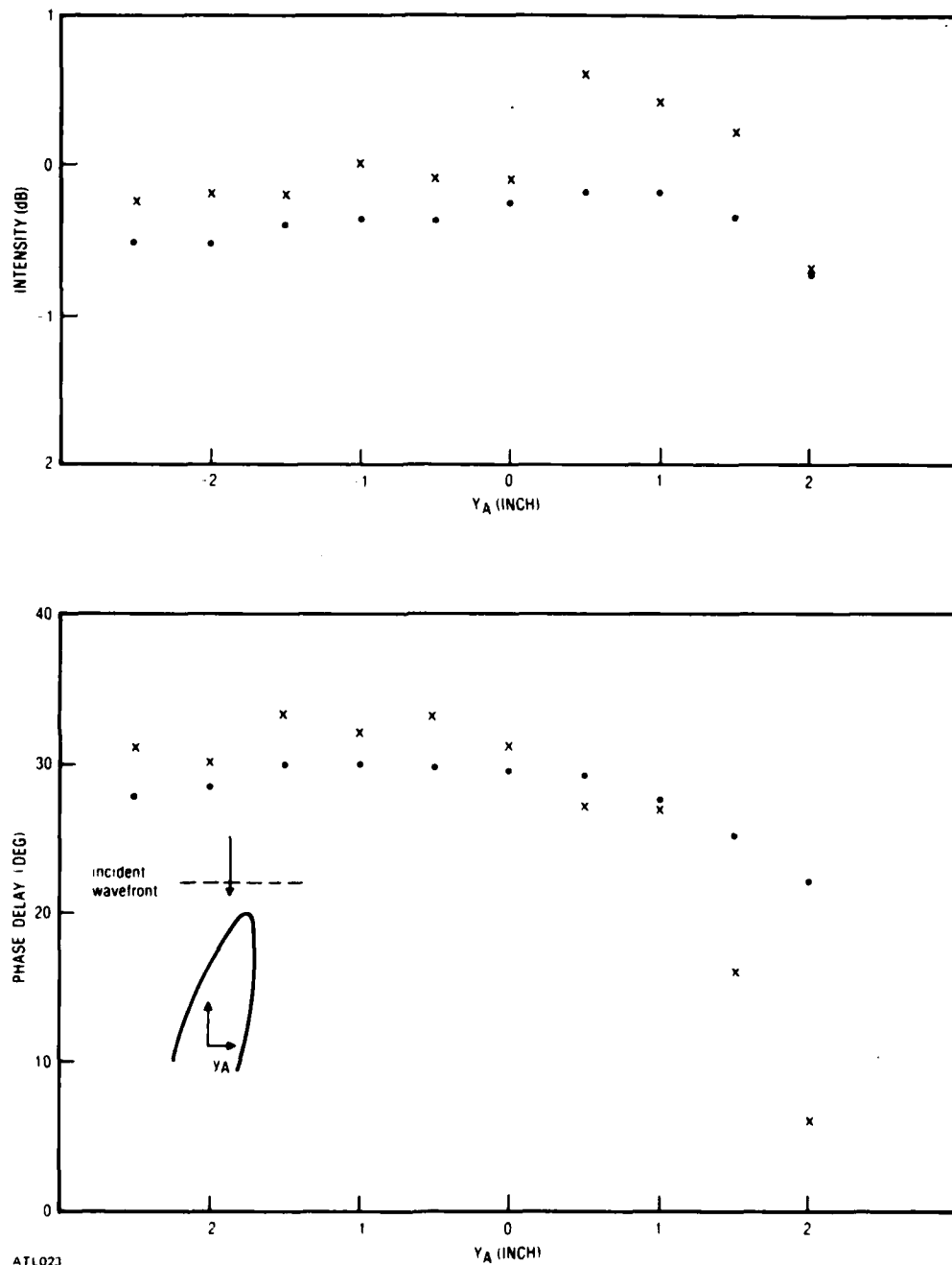Figure 3.4-8. Intensity and Phase Axially Symmetric Shell for $\beta = 15°$; E-Plane. Measured with 1.25-in. square antenna (x). Calculated with surface integration ($\cdot$) for $\ell = 40\lambda$; frequency 10 GHz.
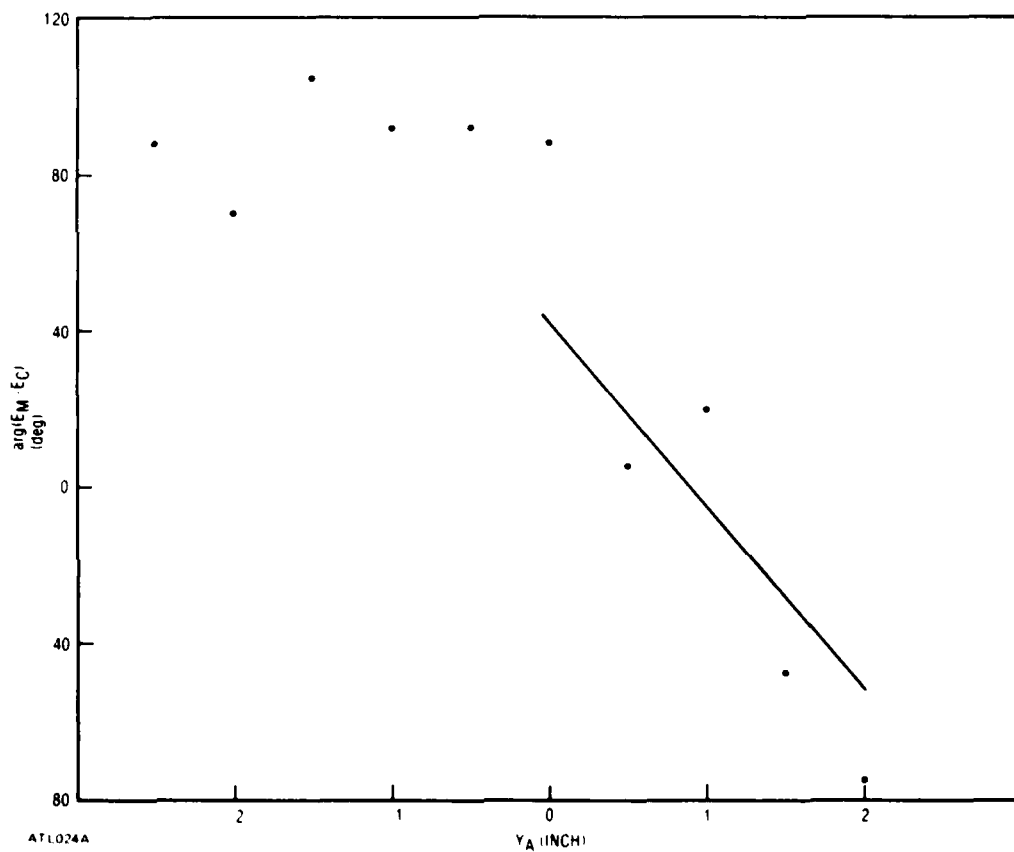
3-25
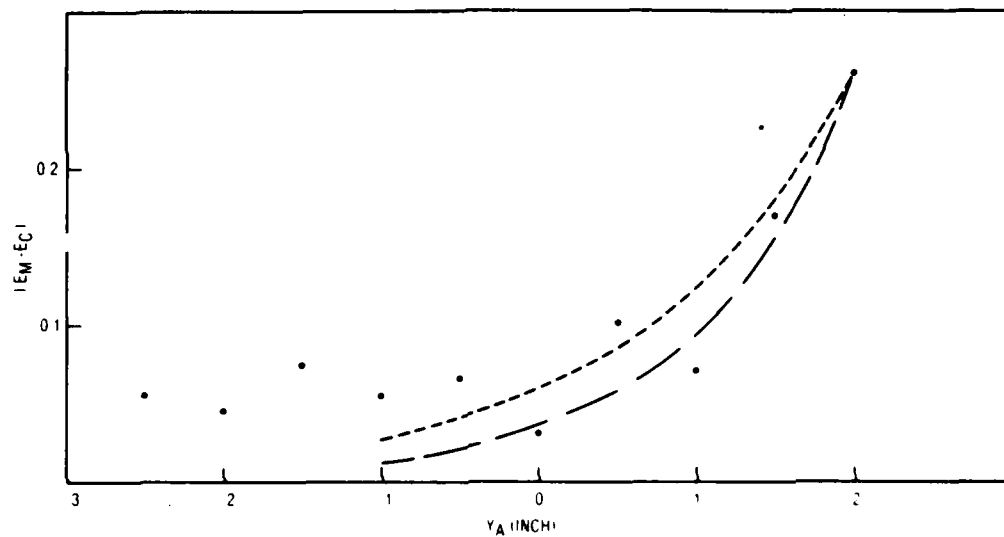
Figure 3.4-9. The Magnitude and Phase of $E_m - E_c$ (•). Computed values of $0.260 \exp(-v|y_A - 2|)$; for thickness 0.125 in. (- - - -); for thickness 0.150 in. (-- --).

ATL024A

3-26

$(k_g \, y_A \, \sin \theta \,)$ is superimposed on the phase values of $E_m - E_c$ in Figure 3.4-9; the location of the line on the ordinate scale is arbitrary: the slope is significant.

The comparison of computed and measured phase in Figure 3.4-9 further confirms the view that the field near the wall of the shell contains a constituent that is a guided wave, and the constituent is a slab-guided wave.

This model omits the opposite radome wall and a backward propagating guided wave as an approximation. Furthermore, the model does not acknowledge the dependence of guided wave excitation on gimbal angle; this dependence for slabs has been established in our earlier work with the moment method. Although $E_m - E_c$ has been calculated for additional gimbal angles, we omit the results for brevity.

It is useful to state that v is larger for perpendicular polarization than for parallel. Consequently, the exponential function decreases less rapidly for parallel polarization. We expect guided wave effects to be more pronounced in E-plane data.

In addition, the gimbal angle β plays a role. For β as in Figure 3.4-10, the phase of $E_m - E_c$ decreases with Y_A (Figure 3.4-9) because the points on the probing path move nearer the source of the wave as Y_A increases. For smaller offset angles, the phase surface tilts so that β is negative and phase increases Y_A. This behavior explains the sign reversal in the boresight error curve of Figure 3.4-6, which is for the E-plane. For the H-plane the value of v is 2.21/inch for thickness 0.125 in.; the guided wave is strongly attenuated.

Figure 3.4-10. A Suggestion of a Guided Wave on a Slab that Approximates the Side of the Radome Near Y_A and Equals 2-In. in Figure 3.4-6

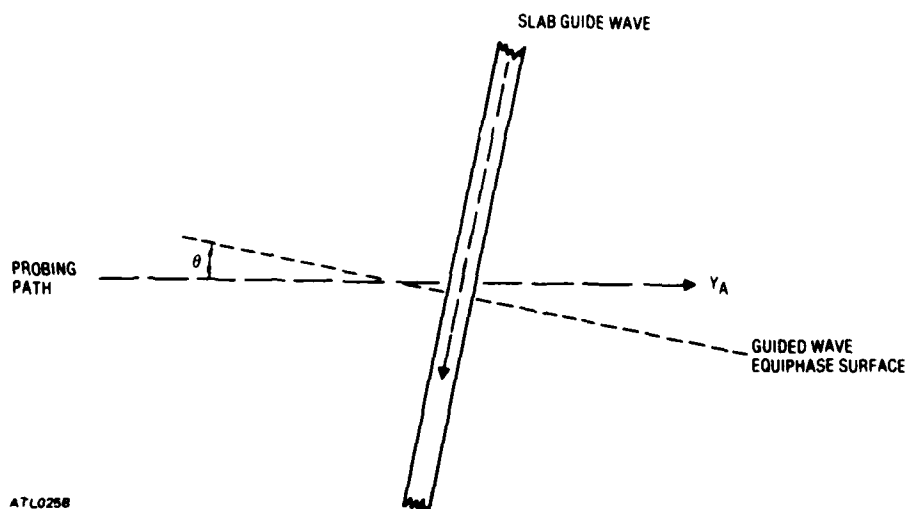# 4. HOLLOW FINITE CYLINDER

Fields near a finite dielectric cylinder were computed using the new version of a moment method theory outlined in Section 2. This new version includes an axial component, as well as transverse components, of field near the scatterer. The newer theory gives better agreement with measured nearfields than did an older theory that omitted the axial component. Polarization dependence is correctly computed.

4.1 COMPUTATIONS

The fields near a hollow finite cylinder were computed for axial incidence. The dielectric constant was 2.6, outside diameter was 1.25 in., thickness was 0.065 in., and length was 0.42 in.

To test the effect of cell size upon the fields, two cylinders like those in Figure 4.1-1 were used to evaluate the equations of the preceding section. Each cylinder was divided into two rings. The first cylinder had 16 cells per ring; N was 32 for the entire cylinder. The second cylinder had 32 cells per ring; N was 64. The external field at 1.26 in. from the center of the ring was computed for cylinder one (Figure 4.1-2).
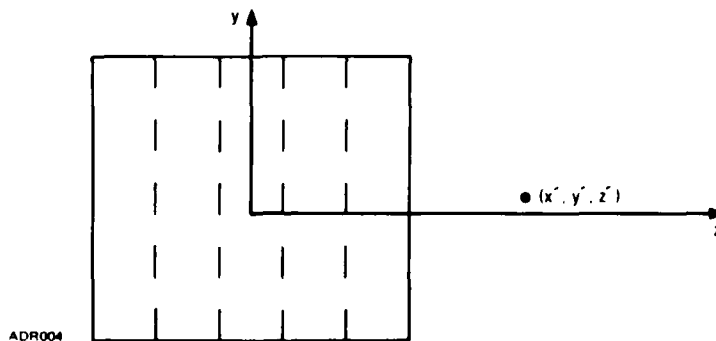
Figure 4.1-1. Subdivision of Hollow Cylinder into Rings. An observation point has coordinates (x', y', z'); it may be inside or outside the cylinder.

Calculations for the second cylinder (N = 64) are shown in Figures 4.1-3 and 4.1-4 for distance 1.26 in., and in Figures 4.1-5 and 4.1-6 for distance 0.63 in. The calculated values are for the equations in Section 2, with $E_z \neq 0$, and for the equations of Reference 3, with $E_z = 0$. The inclusion of E_z and the value of N influence the results.

4.2 DISCUSSION

Figures 4.1-2 through 4.1-6 show measured as well as computed values. The measurements were made by scanning a half-wave dipole probe on horizontal and vertical lines (H- and E-planes).

4-1
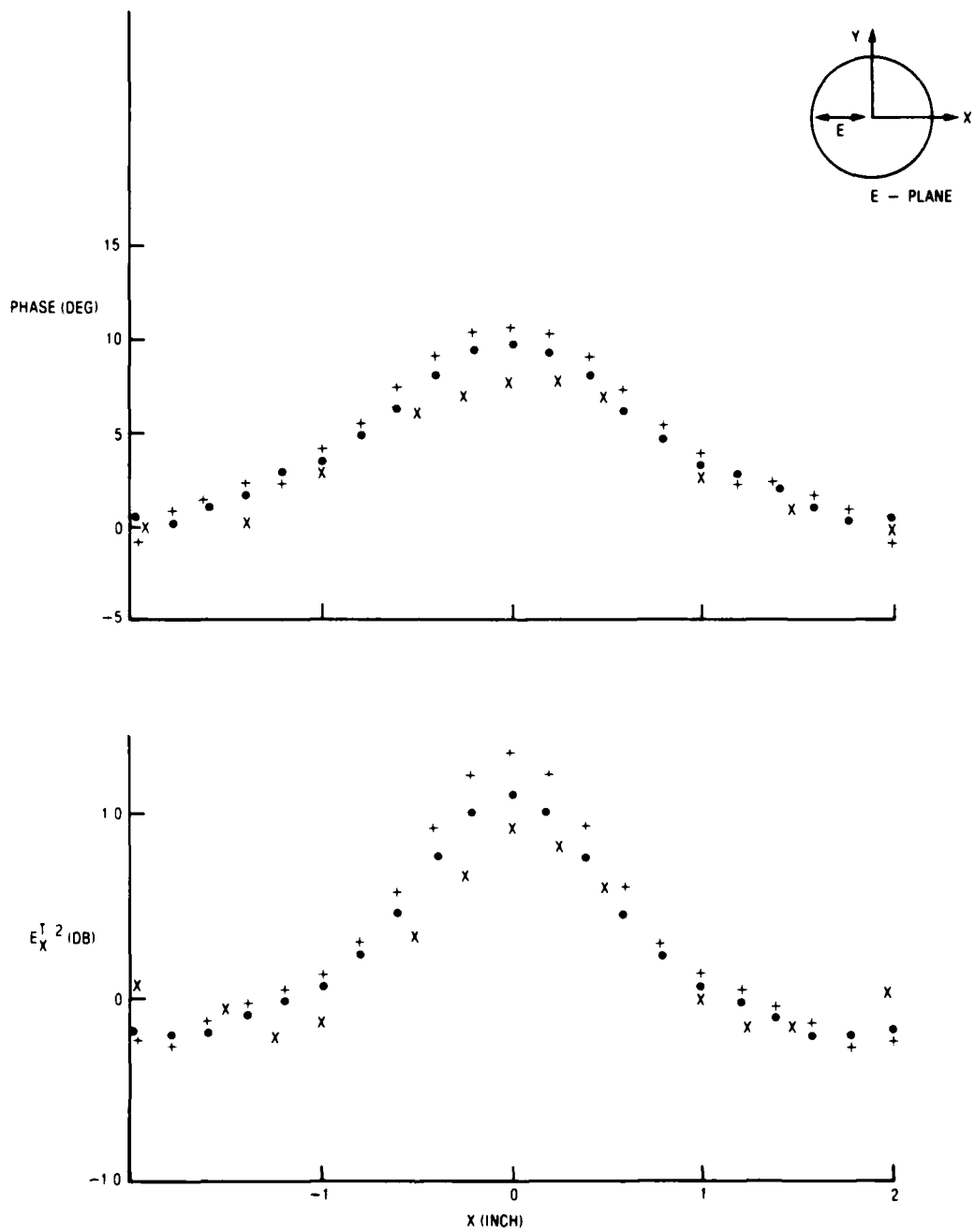
Figure 4.1-2. Total Field at z = 1.26 in. for 0.42 in. Long Ring. Measured (x); calculated, N = 64, $E_Z \neq 0(\cdot)$; calculated, N = 32, $E_Z \neq 0(+)$. Wavelength: 1.26 in. dielectric constant 2.6; diameter 1.25 in.
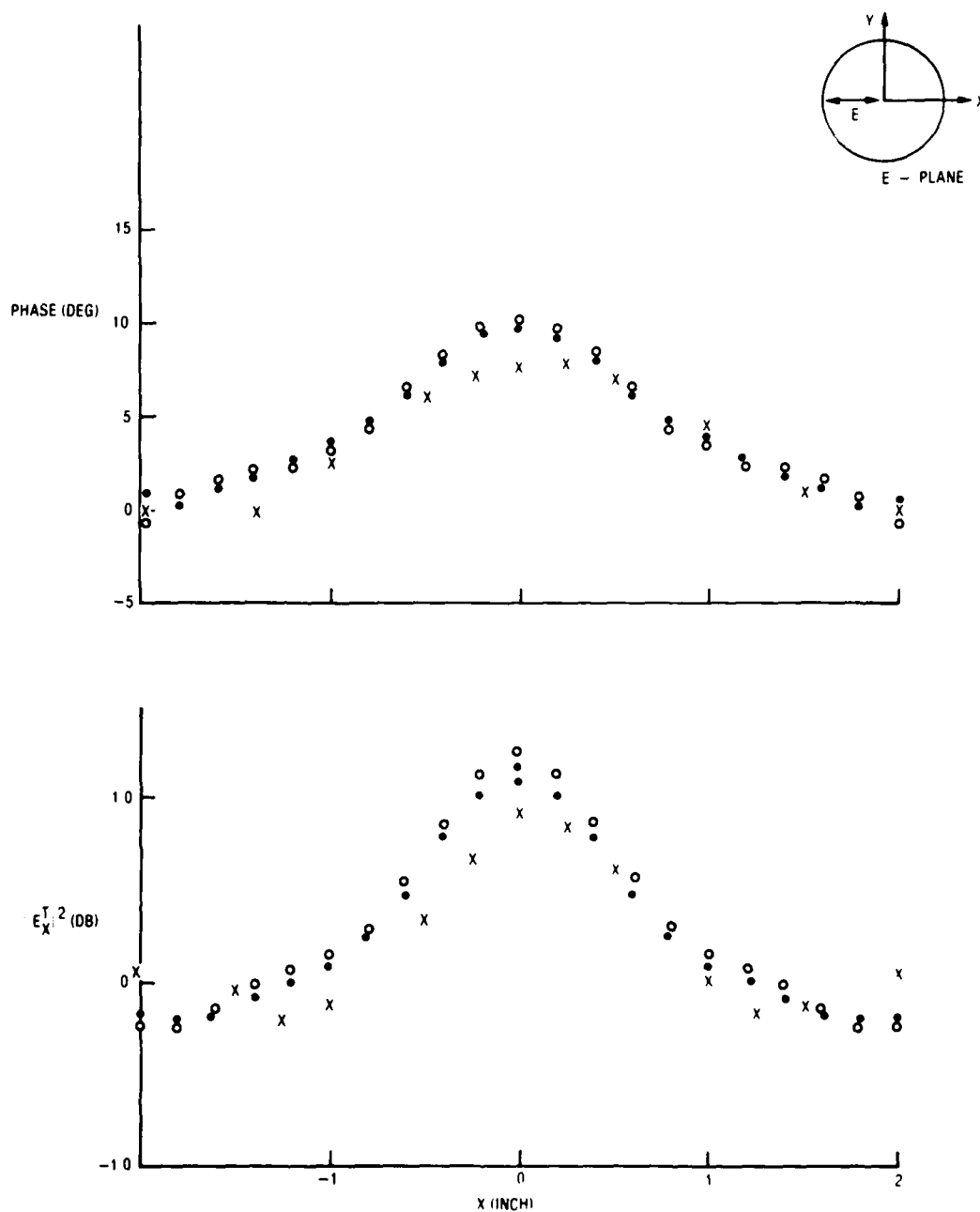
Figure 4.1-3. Total Field at z = 1.26 in. for 0.42 in. Long Ring. Measured (x); calculated, N = 64, E_z = 0 (0); calculated N = 64, $E_z \neq 0$ (•). Wavelength: 1.26 in. Dielectric constant: 2.6 diameter 1.25 in. Calculations: 32 cells/axial subdivision
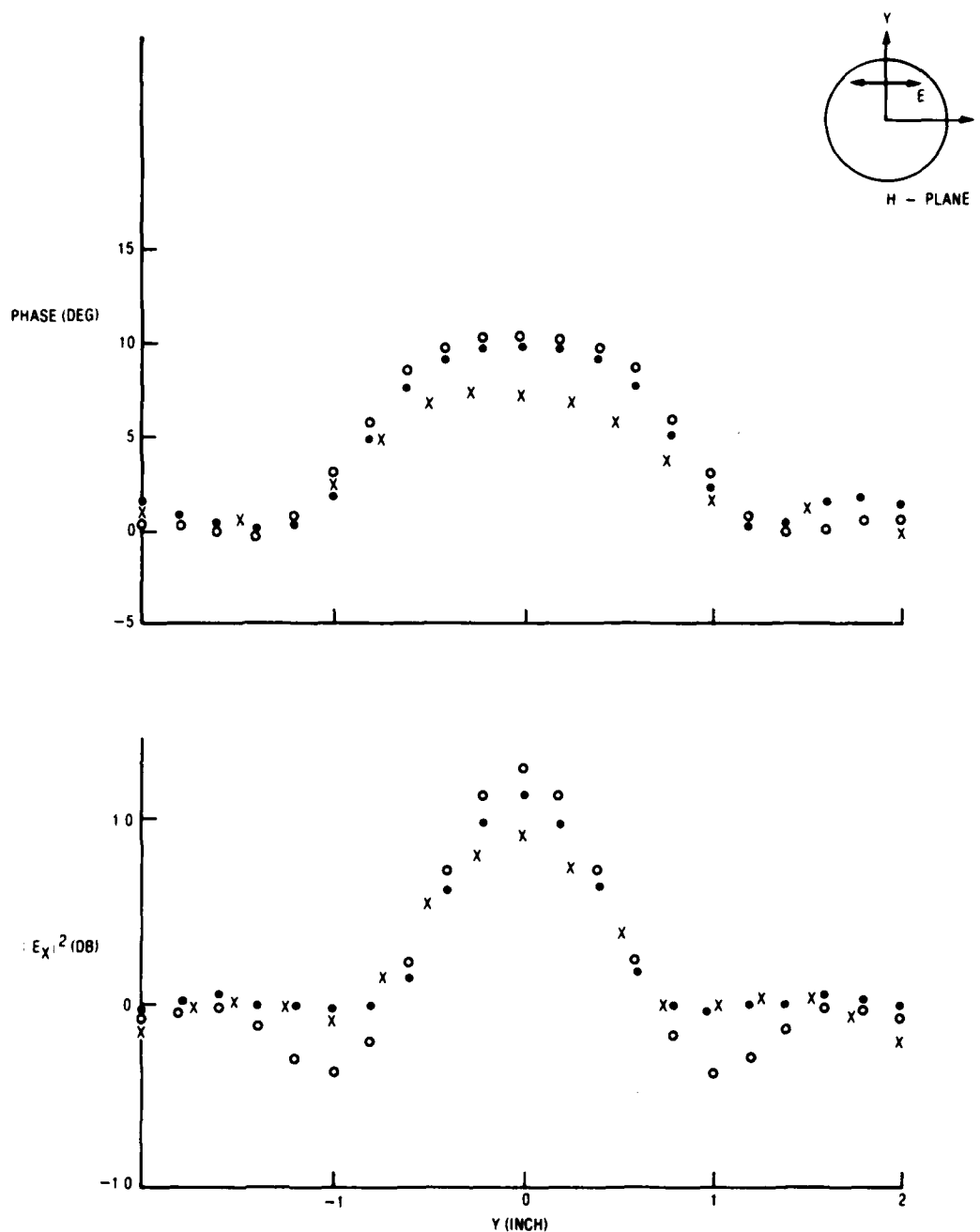
Figure 4.1-4. Total Field at z = 1.26 in. for 0.42 in. Long Ring. Measured (x); calculated, N = 64, $E_z = 0$ (0); calculated N = 64, $E_z \neq 0(\cdot)$. Wavelength: 1.26 in. Dielectric constant 2.6, diameter 1.25 in. Calculations: 32 cells/axial/subdivision

4-4
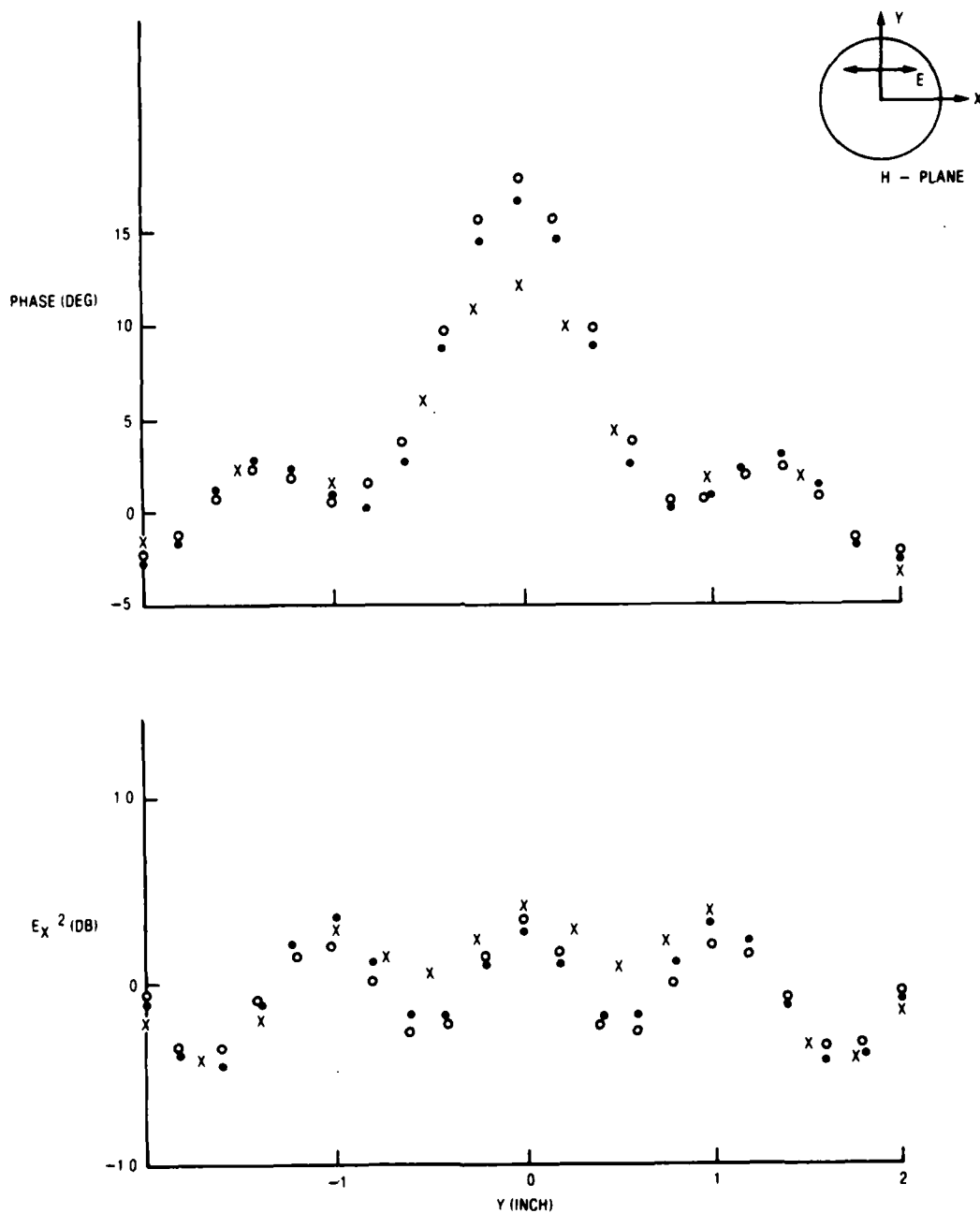
Figure 4.1-5.   Total Field at z = 0.63 in. for 0.42 in. Long Ring.   Measured (x);
               calculated, N = 64, $E_Z = 0$ (0); calculated N = 64, $E_Z \neq 0$ (•).
               Wavelength: 1.26 in.   Dielectric constant 2.6, diameter 1.25 in.
               Calculations: 32 cells/axial/subdivision
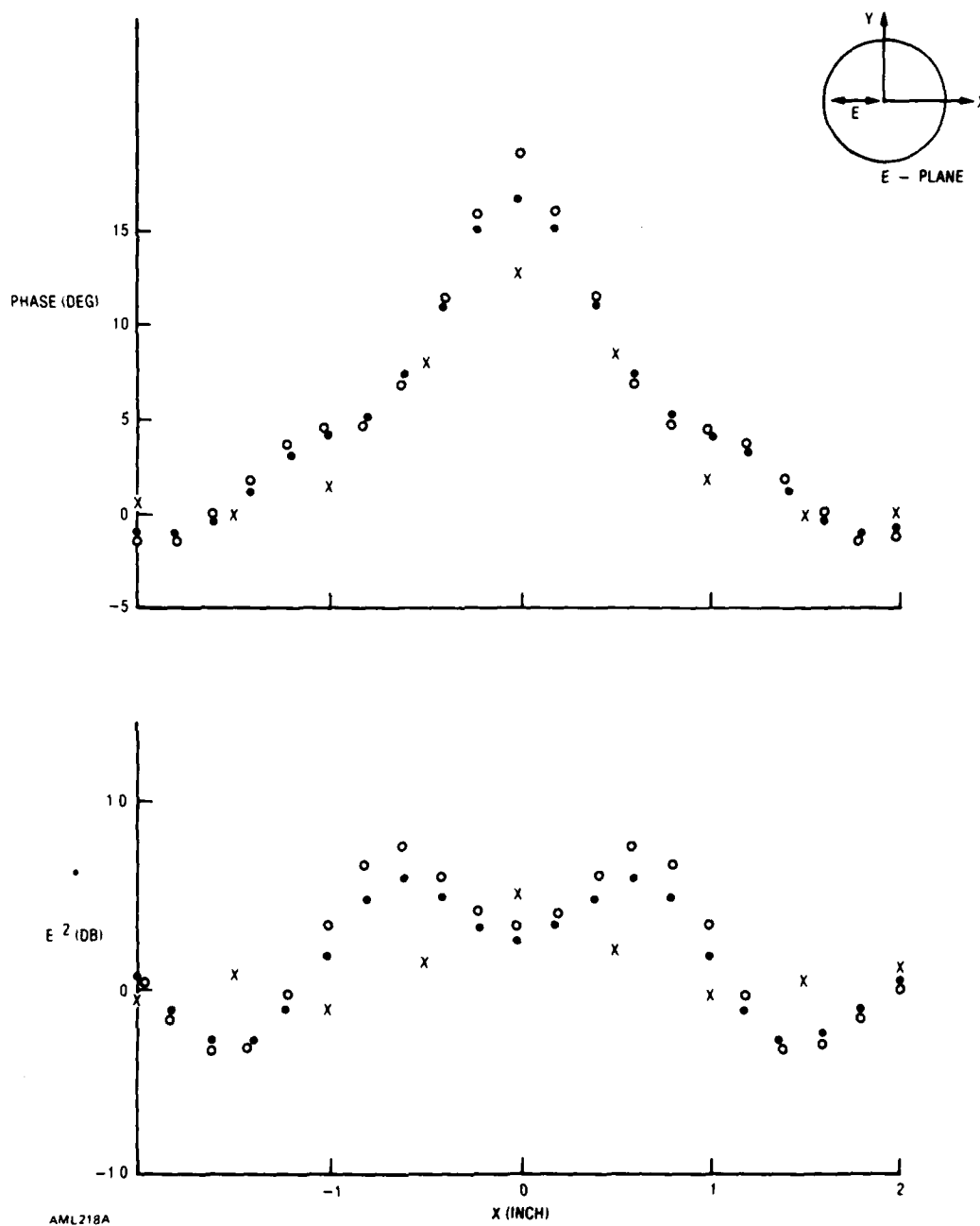
Figure 4.1-6. Total Field at $z = 0.63$ in. for 0.42 in. Long Ring. Measured (x); calculated, $N = 64$, $E_z = 0$ (0); calculated $N = 64$, $E_z \neq 0$ ($\cdot$). Wavelength: 1.26 in. Dielectric constant 2.6, diameter 1.25 in. Calculations: 32 cells/axial/subdivision

Figure 4.1-2 shows that the discrepancies between measured and computed values are smaller for N = 64 than for N = 32.

Figures 4.1-3 and 4.1-4 show discrepancies are smaller for the equations with $E_z \neq 0$ than they are for $E_z = 0$. The same conclusion follows from Figures 4.1-5 and 4.1-6.

Accuracy is good in Figures 4.1-3 and 4.1-4 where the distance between the probe and scatterer is a wavelength. Notice that the spatial dependence in the E-plane (Figure 4.1-3) differs from that in the H-plane (Figure 4.1-4). Accuracy is not as good when the probe-scatterer distance is half a wavelength (Figures 4.1-5 and 4.1-6). Reference 5 showed that on-axis discrepancies were reduced by introducing a probe correction.

5. HOLLOW CONES

This section presents data for measured and computed fields for a hollow cone for the two versions of the moment method theory ($E_z = 0$, and $E_z \neq 0$) outlined in Section 2. The results are for axial and nonaxial incidence.

It was shown in the preceding sections that the shapes and sizes of the cells into which a dielectric structure is decomposed influence computations. Accuracy depends on cell size because of the assumption that the field in a cell is constant; therefore, smaller cells are desirable. However, computation increases with decreasing cell size, and eventually cell sizes can be made so small that the storage capacity of computers may be inadequate to solve the large set of simultaneous equations. In addition, as the cell size is decreased, the computed fields might not converge to a reasonably fixed distribution of values. Finally, cell shape should be chosen to exploit those directions in which the field varies slowly; of course, the cells should fit the scatterer's geometry.

With these limitations in mind, we have chosen for hollow cones a division that is described in Figures 2.2-1, 2.2-2, 5-1, and 5-2. Figure 5-1 is a picture of an experimental model that consists of 15 rings of Plexiglass; another version with 13 rings was also utilized. Figure 5-2 gives dimensions for the 13-ring cone.
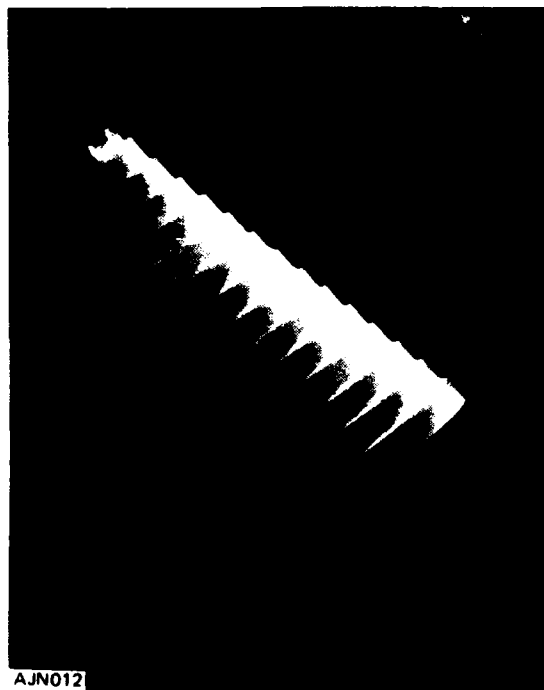

AJN012

Figure 5-1. Hollow Cone Composed of Rings. Half angle is 14°.
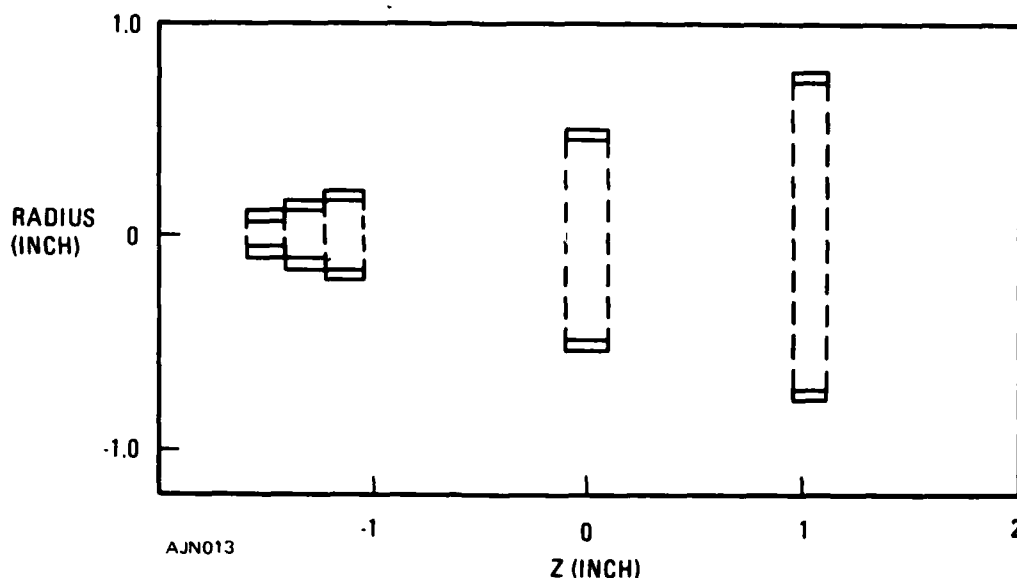Dielectric constant was 2.6.

Figure 5-2. Dimensions of Rings. Cell lengths $2\delta z$ were 0.215 in. Thickness $2\delta p$ were 0.065 in. This figure shows only five of the rings, but the models had either 13 or 15. Overall dimensions in this figure are for a cone with 13 rings.

5.1 COMPUTATIONS AND MEASUREMENTS FOR HOLLOW CONE

This section describes calculations and measurements for a 13-ring cone with the dimensions in Figure 5-2. Results are given for theory with $E_z \neq 0$, and $E_z = 0$, for axial and nonaxial incidence.

Phase and intensity were measured with a half-wave dipole antenna in the region bounded by the cone and over planes behind the cone. The receiver was a network analyzer; its reference field propagated through a waveguide. The transmitting and receiving antennas were spaced by 100 inches. The cone was suspended by nylon threads in an anechoic chamber.

The procedure for positioning the probe relative to the cone was to start with the probe at a specific axial distance from the base and to scan the probe laterally. Axial position was changed and scans repeated. The cone was stationary. To obtain data for the incident field the cone was removed. This procedure was more accurate than an earlier procedure in which the cone was removed or replaced between scans and axial probe displacements.

Figure 5.1-1 shows computed values of $|E|^2$, the intensity corresponding to the total internal field, for axial incidence, on two cone generators. One generator is in the x-z plane, called the E-plane because it contains the electric field. The other generator is in the y-z plane, called the H-plane. Note, that the field in the H-plane is larger than that in the E-plane. The results differ somewhat for the two 13-ring cases. In one case each ring contained 12 cells. In the other case, the six smallest rings had eight cells each, and the seven largest rings had 16 cells each. The main differences are near the tip, within the smaller cells. The smallest rings have thicknesses approximately equal to their radii, a condition which violates an assumption in the derivation of the working formulas. Therefore, calculations were made by representing each of the three smallest rings of the 13-ring cone by a pair of concentric rings and retaining the 10 remaining

CONICAL SHELL INTERNAL FIELD

* 13 rings; 12 cells/ring
□ 13 rings; 8 or 16 cells/ring
x 11 rings; 16 cells/ring

Z (INCHES)

AJN014A
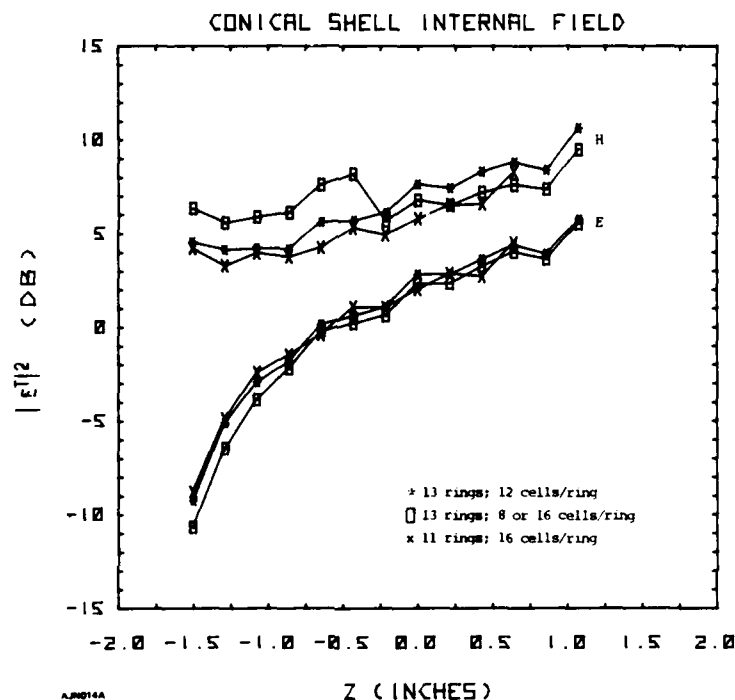
Figure 5.1-1.   Computed $|E|^2$ Inside Conical Shell. The inset shows the loci of points.
E refers to points in the x-z plane, the E-plane; H refers to y-z plane,
the H-plane. Computed for $E_z = 0$.

rings as before. Figure 5.1-2 shows the results. It is clear that the field depends on axial position.

To evaluate the significance of the difference between the internal fields for the two subdivisions, we compared the respective external fields computed for the two sets of internal fields. Figure 5.1-3 shows the measured and computed fields for both sets at one-half wavelength behind the largest ring. Near the main maxima for phase and

5-3
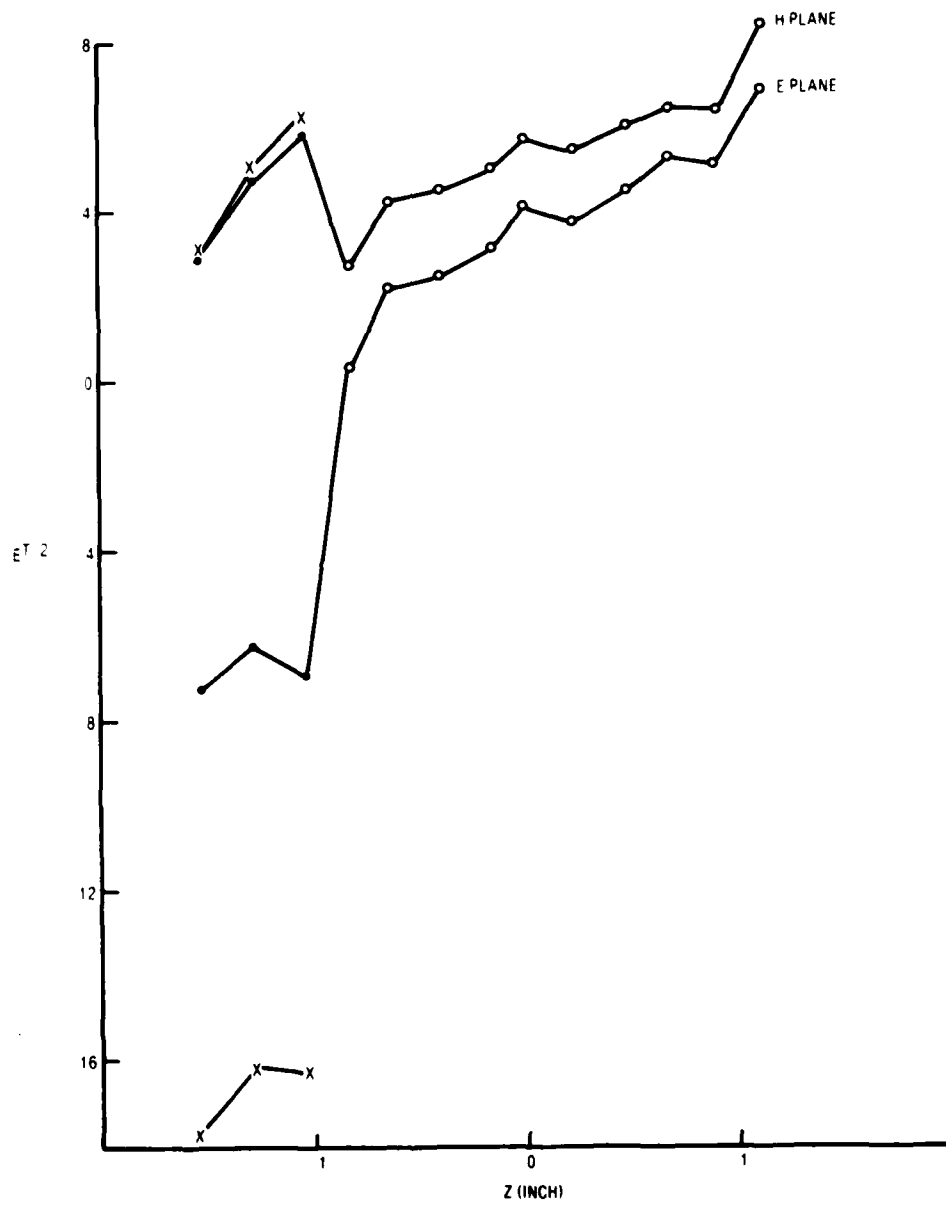
Figure 5.1-2. Computed Internal Field Intensity for Another Subdivision
of Three Smallest Rings. Computed for $E_z = 0$.
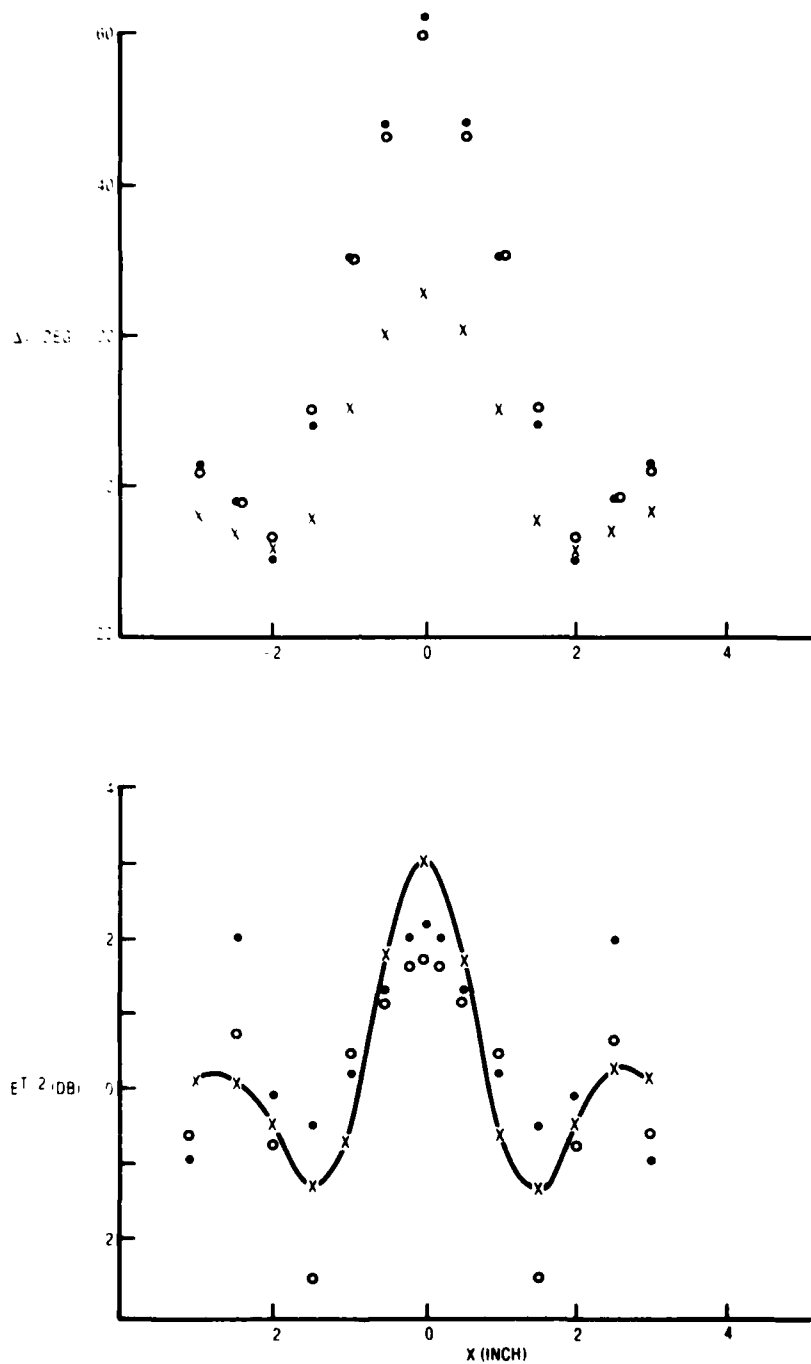
Figure 5.1-3. $|E^T|^2$ at One-Half Wavelength Behind Largest Ring (z = 1.812 in.).
Measured (X); computed (•) for 13 rings, 12 cells/ring $\delta\rho$ = .065 in.;
computed with 16 rings, smallest rings have $\delta\rho$ = .033 in. (o). Computed
with E_z = 0.

AJN035

5-5

intensity, the results agree rather well, but considerable differences exist in intensity at the deepest minimum and the secondary maxima. At the intensity maximum, the discrepancy between the measured value and that computed with 13 rings is approximately 8%; the discrepancy is approximately 15% for 16 rings. The intensity discrepancies at the first minimum and subsidiary maximum favor neither subdivision.

For axial incidence, Figure 5.1-4 shows the measured and computed values of phase delay and $|E_x|^2$, the intensity corresponding to the x component of field. The field was evaluated at z = 0.86 in., which is the plane of the center of the 12th ring, that next to the largest. The results are for both the E and H planes, and for E_z = 0 and $E_z \neq 0$.

For nonaxial incidence (z = 0.86 in.) Figure 5.1-5 shows $\Delta\Phi$ and $|E_x|^2$ for the incident wave normal at 14.9° to the cone axis. Incidence is nearly grazing on one side of the cone. For axial incidence, Figures 5.1-6 and 5.1-7 show the computed results for $E_z \neq 0$ at z = 1.80 in. (half wavelength behind the largest ring) for the E and H planes.

For the plane one half wavelength behind the largest ring, Figures 5.1-8 and 5.1-9 show phase and intensity (normalized to the incident field) for the E- and H-planes for axial incidence. For off-axis incidence (14.9° between the cone axis and incident wave normal). Figures 5.1-10 and 5.1-11 show phase and intensity for the E- and H-planes, respectively, for off-axis incidence.

Figure 5.1-12 gives measured values with the probe antenna on the x-axis at distance half wavelength behind the cone, and Figure 5.1-13 gives measured values at the same distance for the probe on the y-axis. Two sets of values are shown: one set is measurements taken in August 1982; the other set, in August 1980. The intensity data are quite similar, but the phase curves differ. This difference is approximately constant. We attribute it to imprecision in positioning the cone. The quantity $\Delta\phi$ is determined by comparing phases measured with and without the cone. In the 1980 set of measurements, the probe scanned lines at specific axial positions with the cone present; then the cone was removed and the probe repositioned. In the 1982 set, the probe was not moved axially between measurements with and without the cone.

5.2   DISCUSSION

Preceding sections showed that accuracy was greater for calculations that included both the axial and transverse components than for those with only the transverse component.

There was greater accuracy for the probe positioned a half wavelength behind the base of the cone, but for measurements inside the region bounded by the cone, in the plane of the 12th ring, the relative accuracy was less obvious. The effects of the probe may be greater when it is nearer the cone. Figure 5.1-4 shows a strong polarization dependence: $|E|$ and $\Delta\phi$ vary more for the H-plane than for the E-plane. The values of $|E|$ are larger for the H-plane, as expected from Figure 5.1-1.

Figure 5.1-4 also shows that discrepancies in $\Delta\phi$ are smaller for the theory that has $E_z \neq 0$ than they are for the theory with E_z = 0. For $E_z \neq 0$, phase discrepancies range from 0 to 15%; for E_z = 0, discrepancies range from 2 to 25%. However, intensity discrepancies are greater for $E_z \neq 0$, ranging from 3 to 20%, and they equal 10% for E_z = 0.
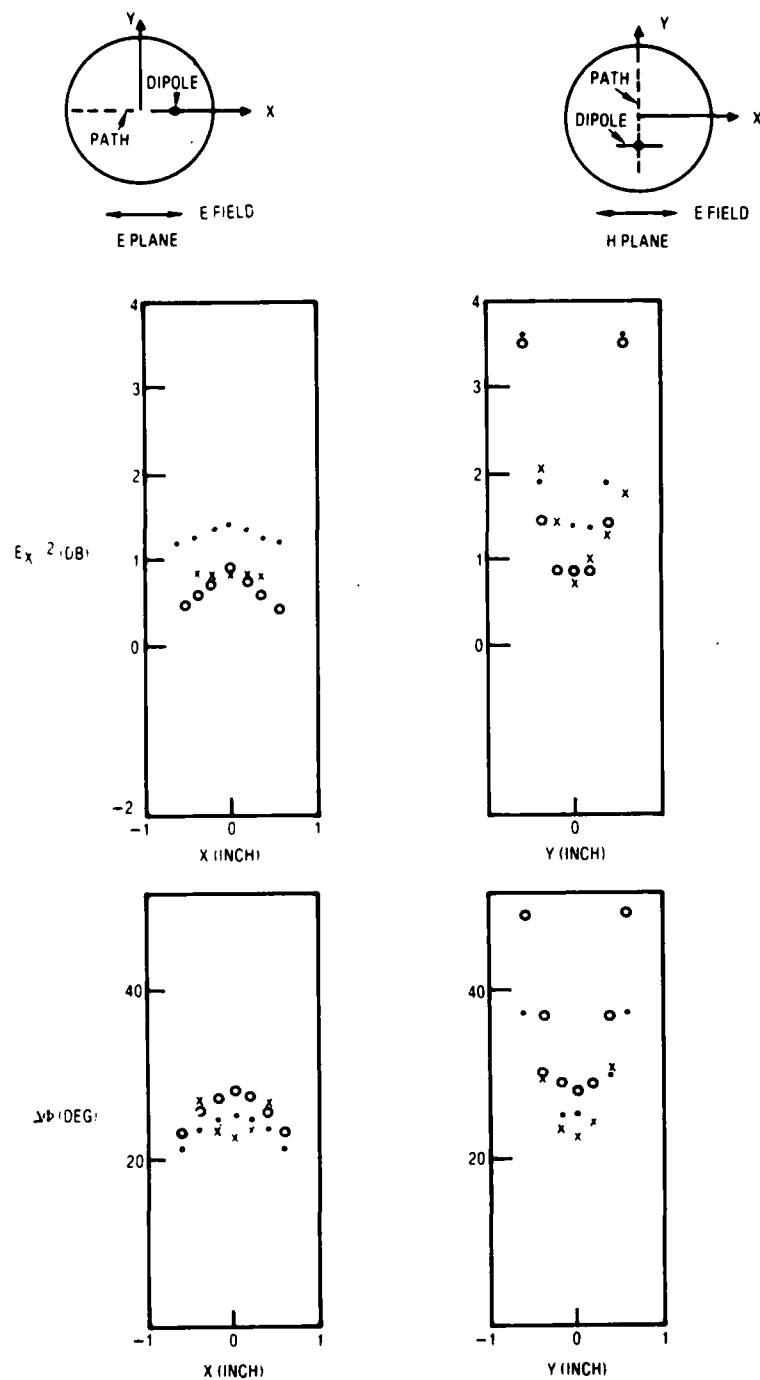
Figure 5.1-4. Phase ($\Delta\Phi$) and Intensity ($|E^T|^2$) Measured (X) and Computed in Plane of 12th Ring (at z = 0.86 in.) for 13-Ring Cone. The electric field was horizontal, in the x-z plane. The H-plane is the y-z plane (x = 0) and the E-plane is the plane y = 0, as shown in the sketches above. The probe was a half-wave dipole. Calculations were done with eight cells per ring. For $E_z = 0$ (o); for $E_z \neq 0$ (·).

E PLANE   H PLANE
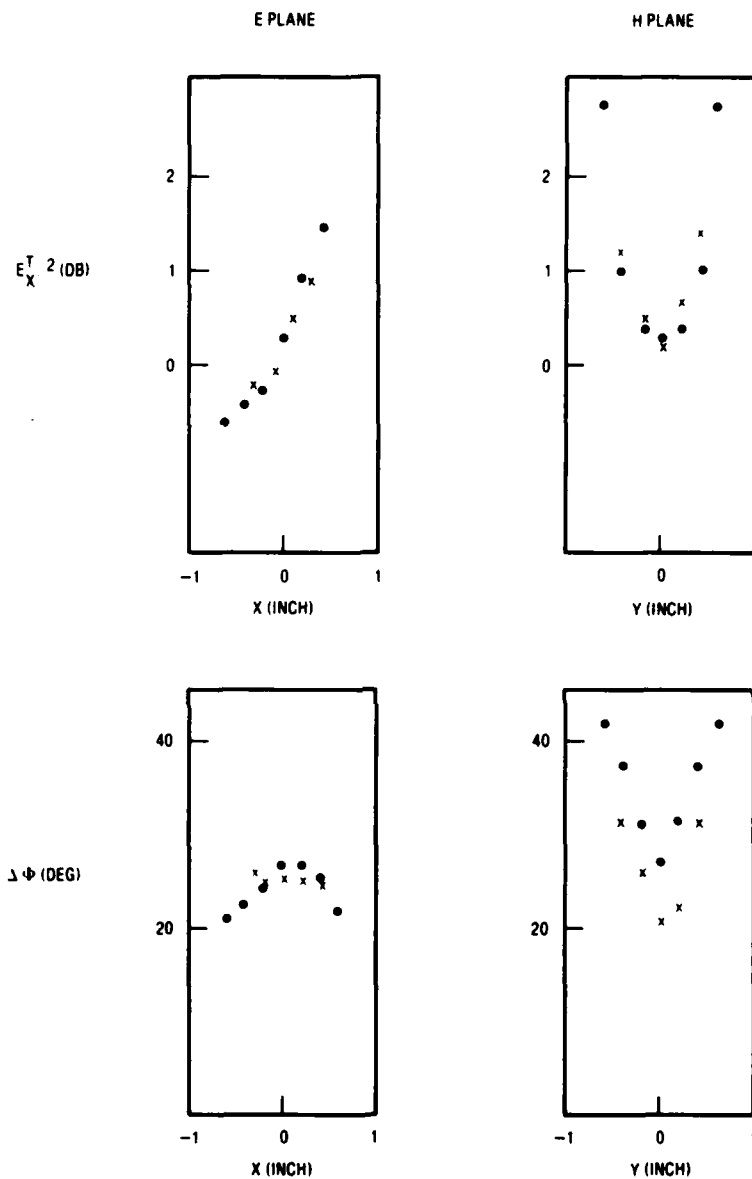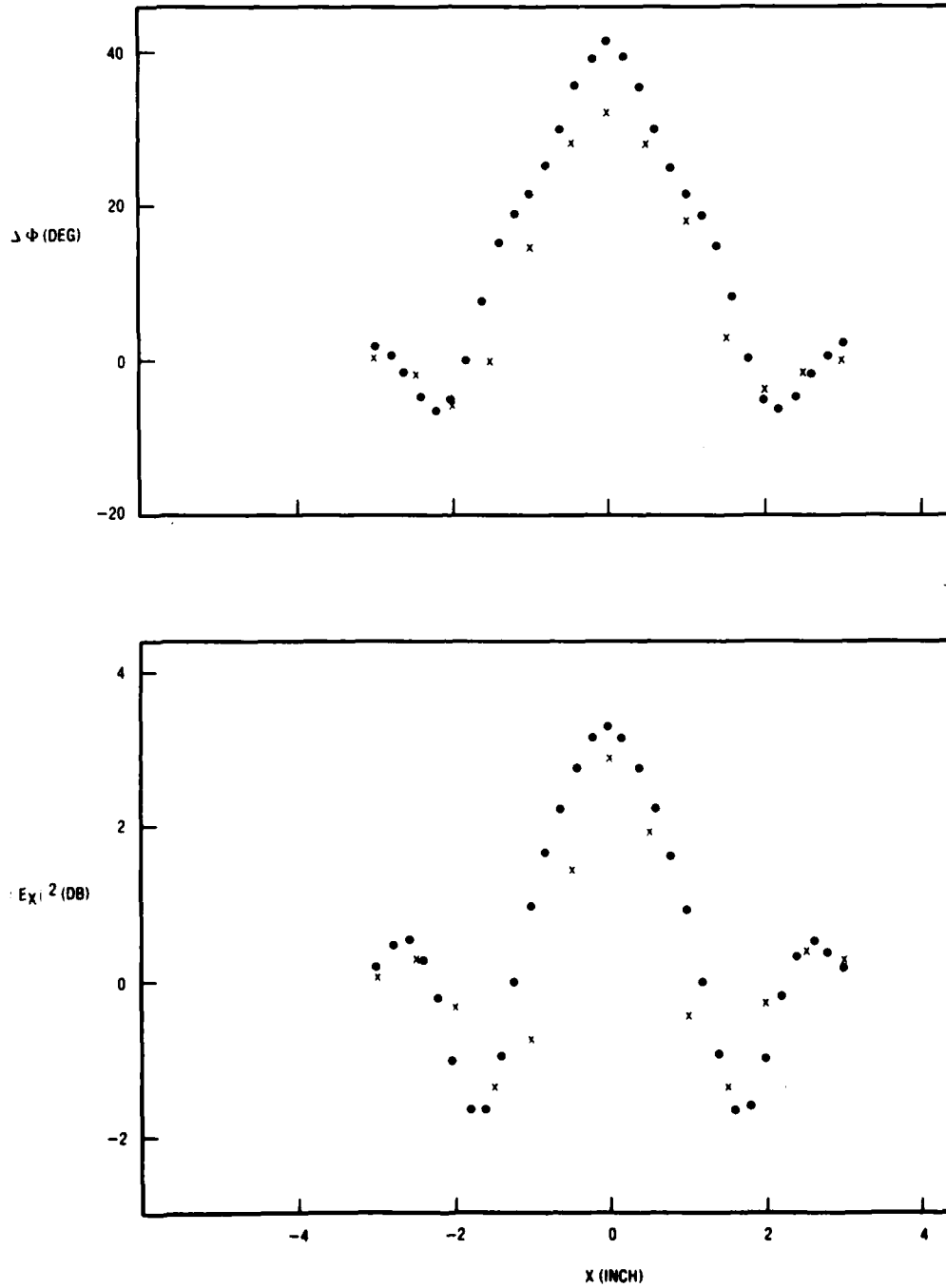

Figure 5.1-5.   Phase ($\Delta\Phi$) and Intensity ($|E|^2$) Measured and Computed in Plane of 12th Ring (at z = 0.86 in.) of 13-Ring Cone, for 14.9° Off-axis Angle of Incident Wave. The E-field was horizontal; E- and H-planes are defined in Figure 5.1-4. The probe was a half-wave dipole. Computed with eight cells per ring. For E_z = 0 (o); for $E_z \neq 0$ (•).

AJN046

Figure 5.1-6. Phase ($\Delta\Phi$) and Intensity ($|E_x|^2$) at z = 1.81 in., a Half Wavelength Behind Largest Ring of 13-Ring Cone. Computed ($\cdot$), with $E_z \neq 0$, with eight cells per ring; measured (x); wavelength 1.26 in. Incidence was axial. Data are for the E-plane.
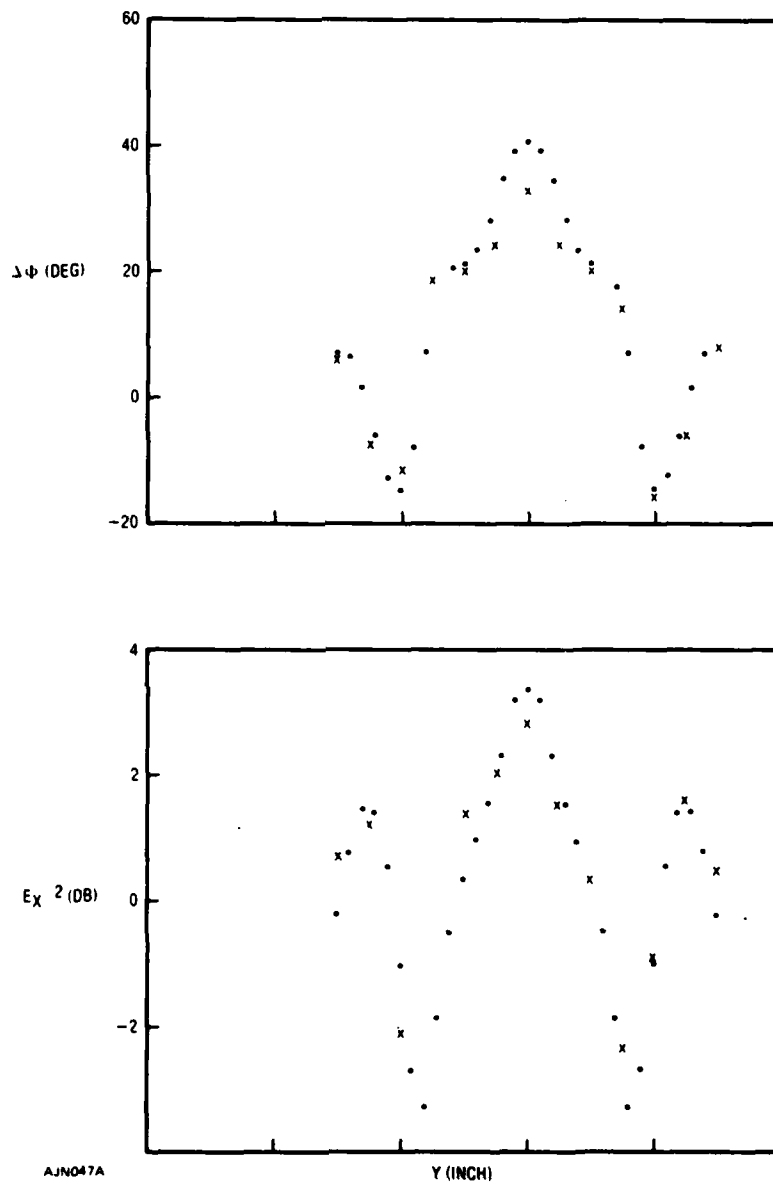
Figure 5.1-7. H-Plane Phase ($\Delta\Phi$) and Intensity ($|E_x|^2$) at z = 1.81 in., a Half Wavelength Behind Largest Ring of 13-Ring Cone. Computed (·), with $E_z \neq 0$, with eight cells per ring; measured (x); wavelength 1.26 in. Incidence was axial.

CALCULATED 8 CELLS/RING $\frac{\lambda}{2}$ BEHIND CONE ● $E_z = 0$
13 RINGS + $E_z \neq 0$
AXIAL INCIDENCE, $\lambda = 1.26$
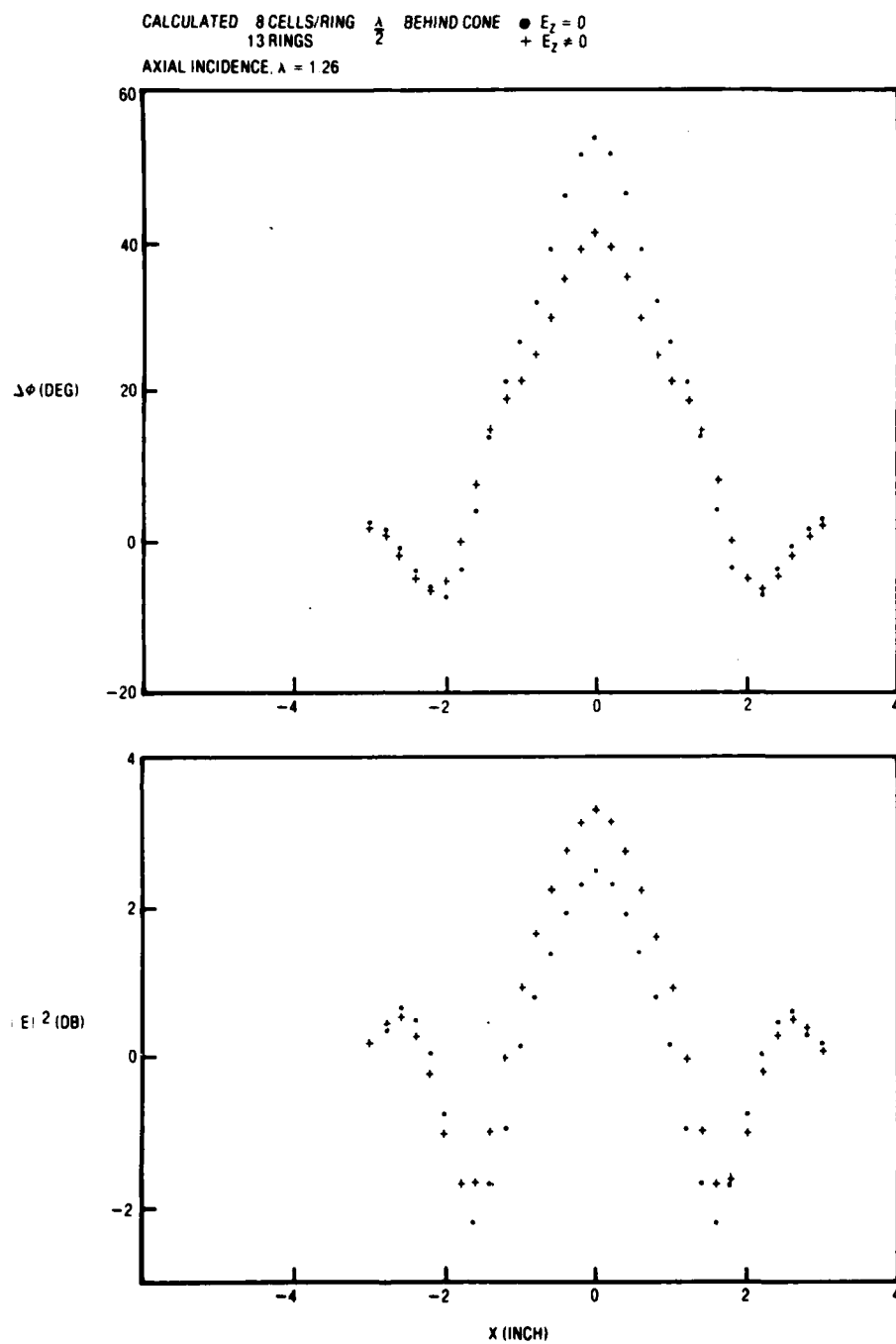
AJN041A

Figure 5.1-8. Phase and Intensity Computed for z = 1.81 in., One Half Wavelength Behind Largest Ring. Computations were done for 13 rings, with eight cells/ring. For $E_z = 0$ (●); for $E_z \neq 0$ (+). E-Plane.

CALCULATED 8 CELLS/RING
13 RINGS
AXIAL INCIDENCE, λ = 1 260'·

● $E_z = 0$

+ $E_z \neq 0$
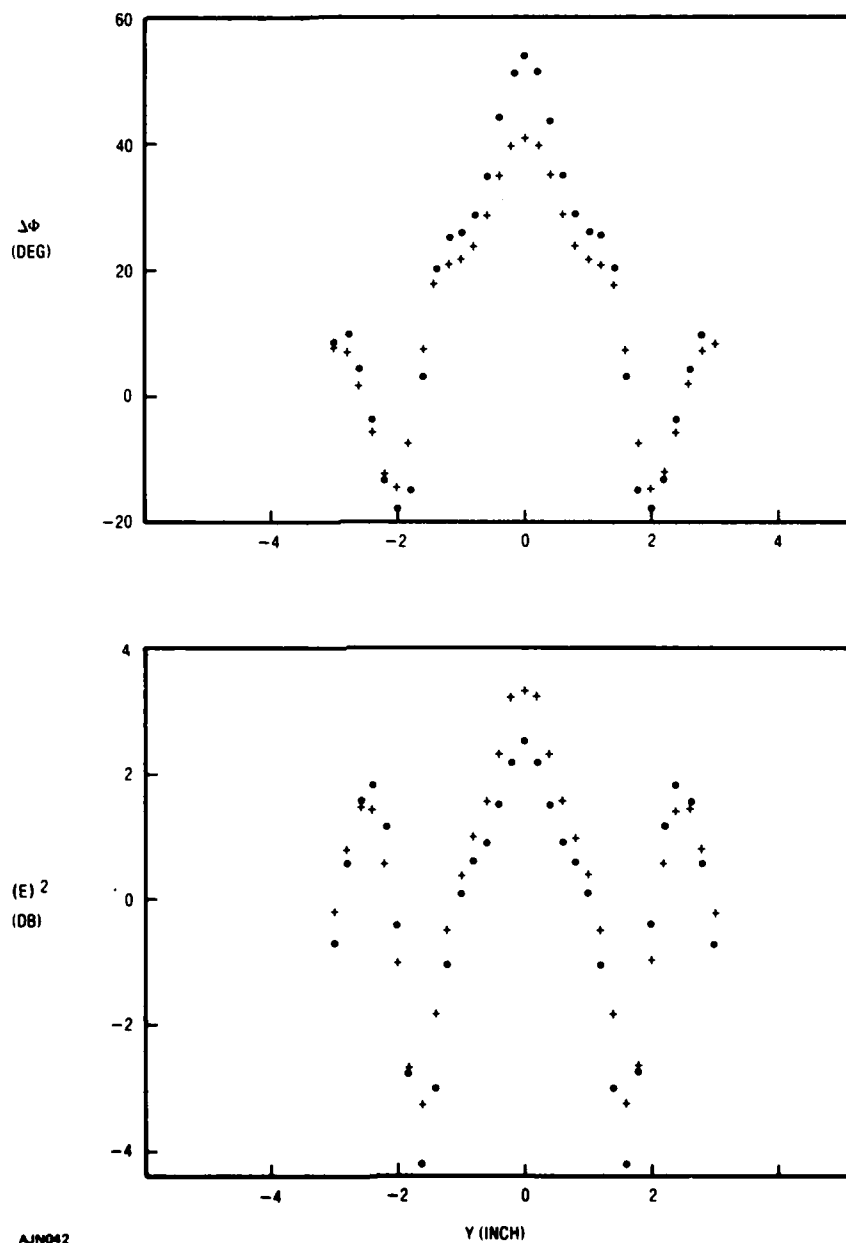
Figure 5.1-9. As in Figure 5.1-8 but for the H-Plane
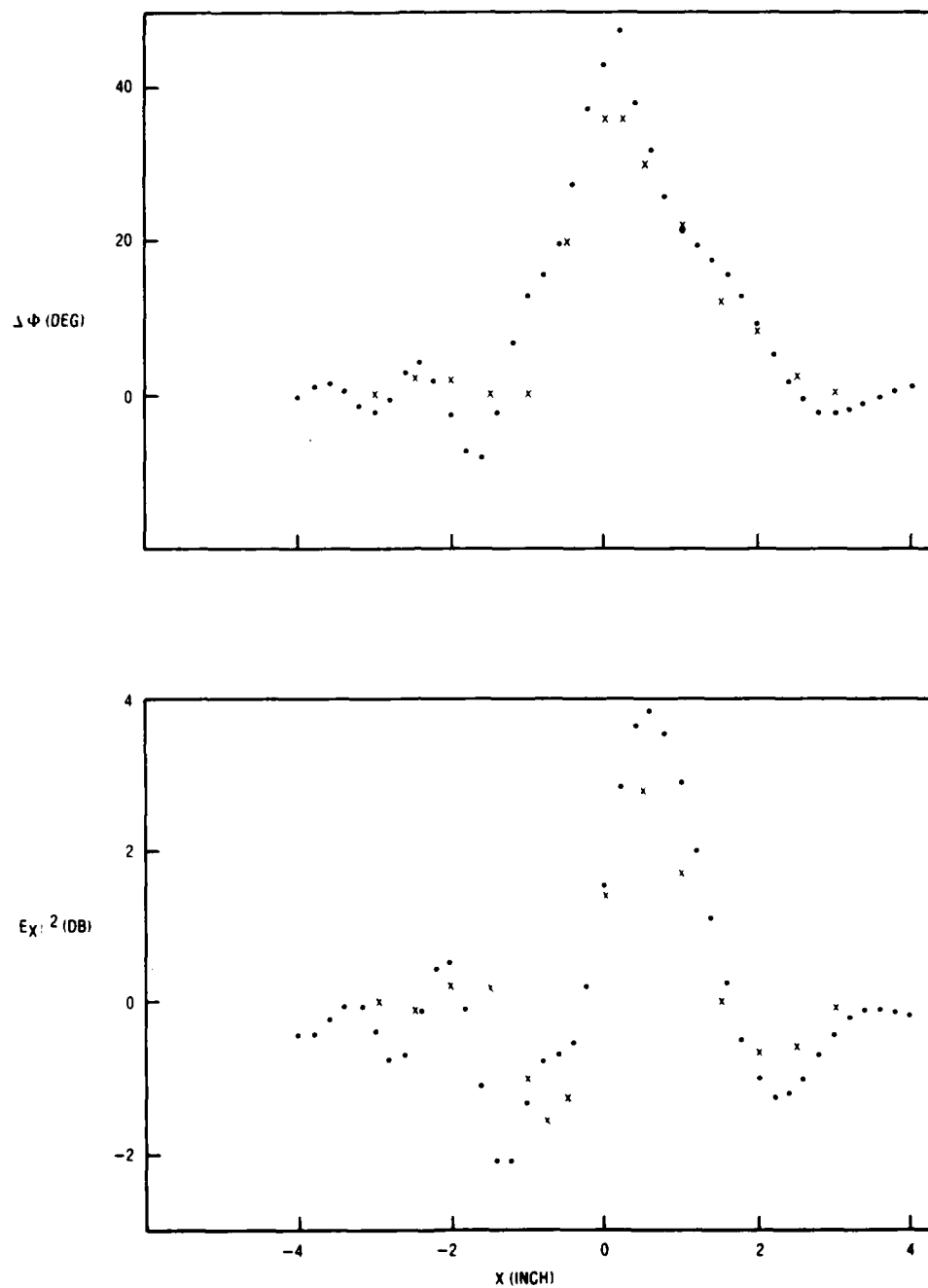
Figure 5.1-10. E-plane, Phase and Intensity at z = 1.81 in. for 13-Ring Cone. Calculated, $E_z \neq 0$ (•); measured (x). The incident wave normal was 14.9° off axis.
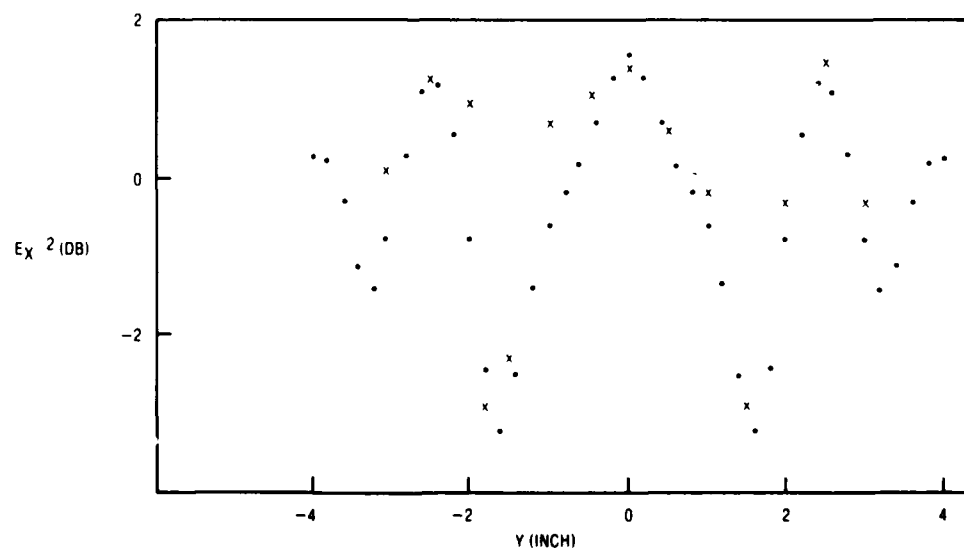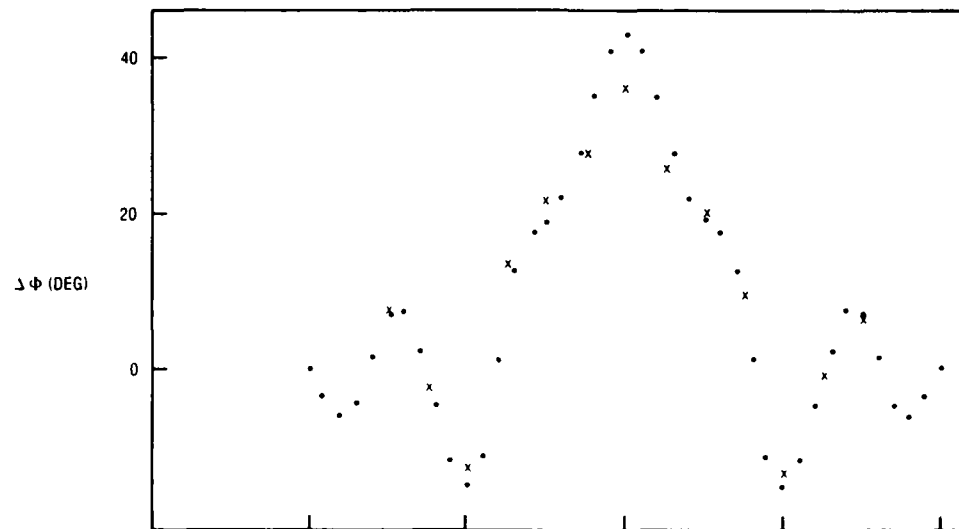
AJN 049

Figure 5.1-11. As in Figure 5.1-10 but for the H-Plane
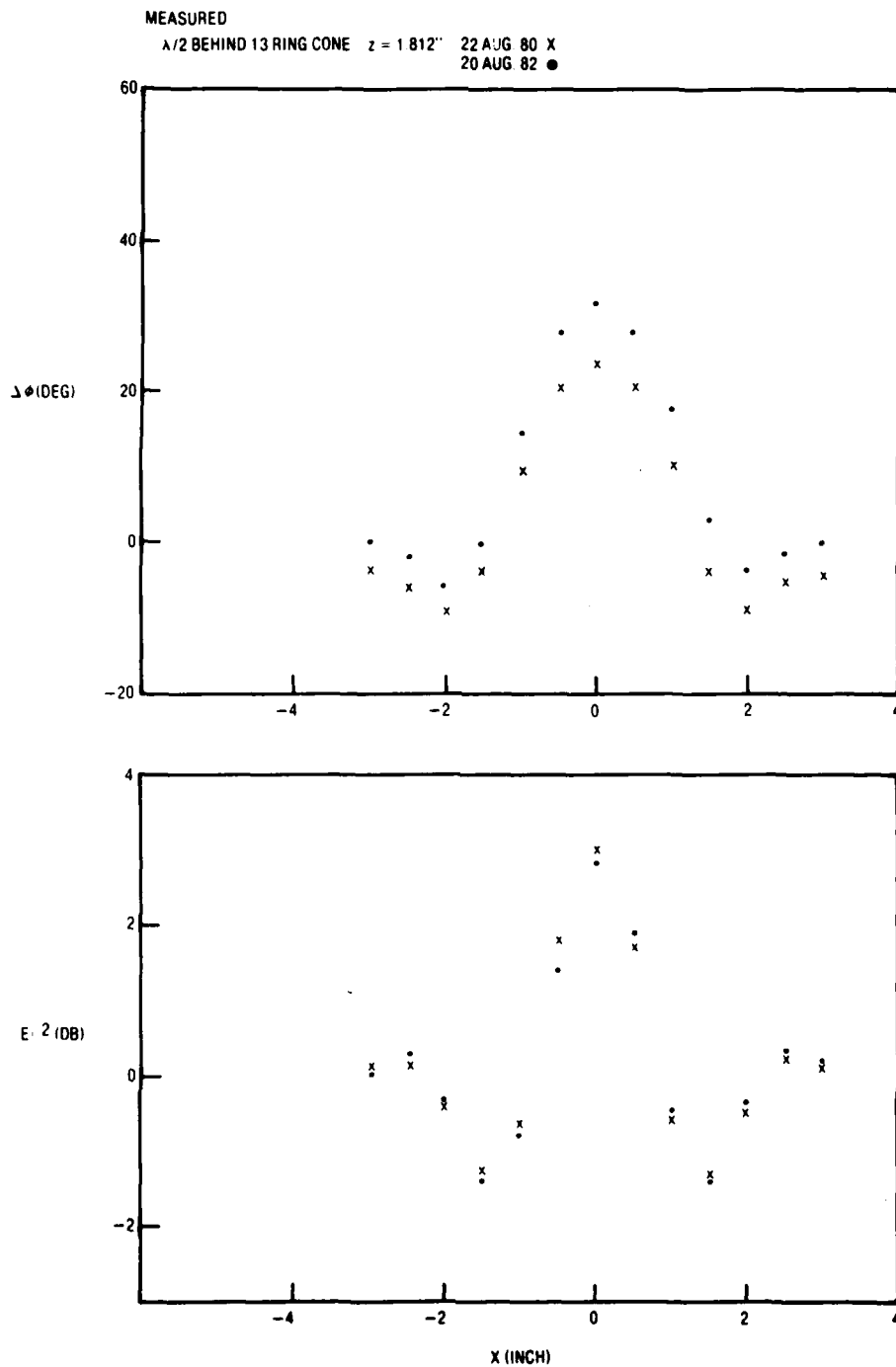
Figure 5.1-12. Measured $\Delta\Phi$ and $|E|^2$

MEASURED
@ λ/2 BEHIND 13 RING CONE   z = 1.812''   22 AUG. 80 X
20 AUG. 82 ●

Figure 5.1-13. As in Figure 5.1-12 but for the H-Plane

AJN044

5-16

For nonaxial incidence, Figure 5.1-5 shows $\Delta\Phi$ and $|E_x|^2$ in the plane of the 12th ring. Discrepancies are small, and the curves have correct shapes. For the E-plane, phase discrepancies are between 2 and 8%. For the H-plane, the discrepancy for the axial position is 30%, and it is 20% for off-axis points; these discrepancies equal approximately 6° in phase. In Figure 5.1-4 the measured and computed graphs of $\Delta\Phi$ for the E-plane have opposite shapes, but discrepancies are still small.

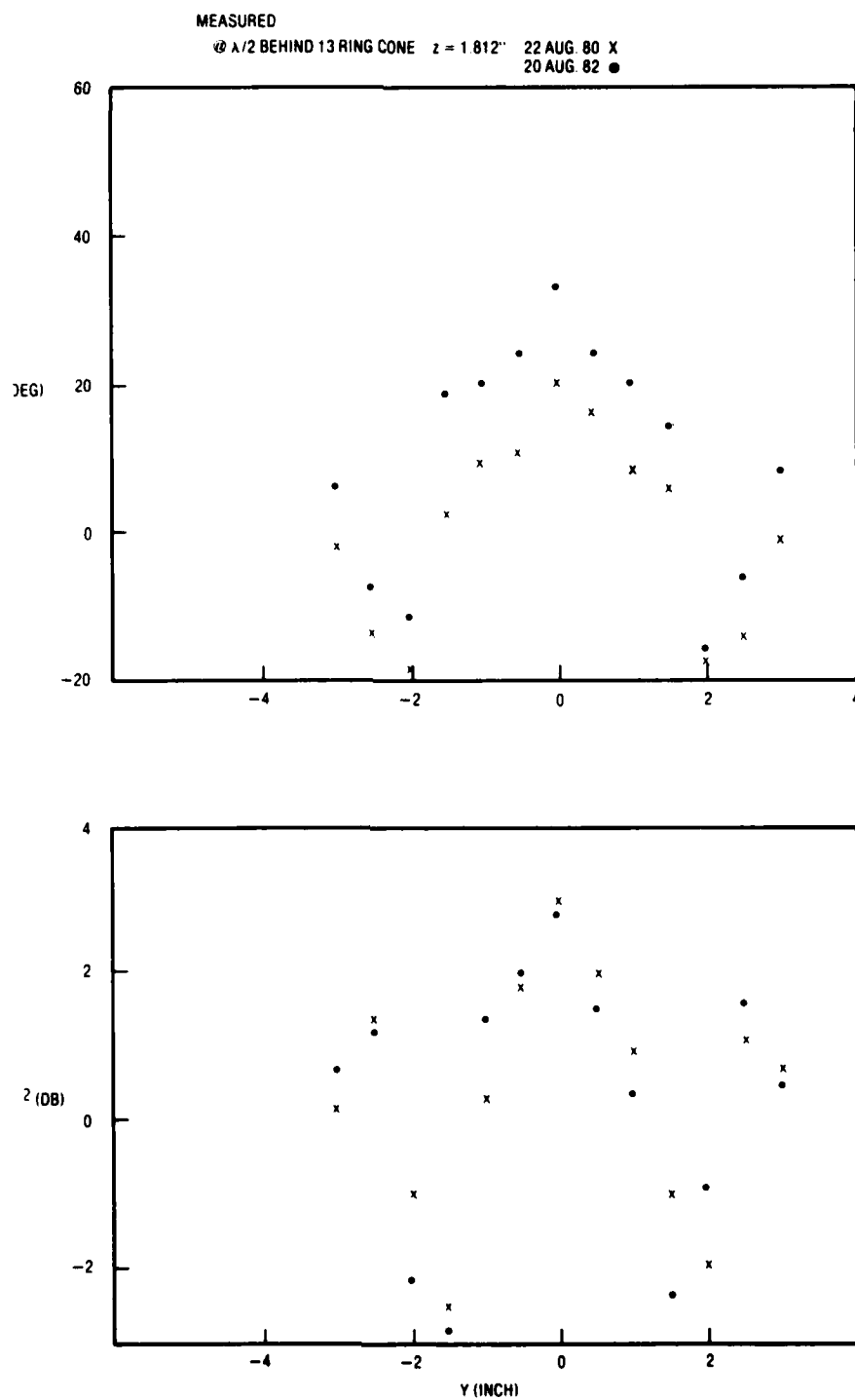Figures 5.1-8 and 5.1-9 show $\Delta\Phi$ and $|E_x|^2$ one half wavelength behind the cone, for axial incidence.

The graphs for the E-plane and the H-plane have different shapes. The secondary maxima for the H-plane are higher than those for the E-plane. Discrepancies of $\Delta\Phi$ for x equal zero are approximately 8°, or 25%. Discrepancies in phase are smaller at off-axis positions, but the percentage discrepancies (ratio of discrepancy to measured value) are large because the values are small. The shapes of the theoretical and measured curves agree well as do locations of extrema.

Figures 5.1-10 and 5.1-11 show $\Delta\Phi$ and $|E_x|^2$ one half wavelength behind the cone, for off-axis incidence. Again the E-plane and H-plane curves have different shapes. The H-plane intensity maxima at off-axis positions are as high as that for the axial position (y equals zero); however, the E-plane intensity maximum at x equal 0.5 in. is much higher than the subordinary maxima. The phase and intensity plots are symmetric in the H-plane, but in the E-plane the off-axis incidence skews the data. The maximum is shifted from the axis toward the direction of the advancing wave normal. The theory agrees well with the measurements although at the discrepancies phase maximum in Figure 5.1-10 are 30%. In Figure 5.1-11 the phase discrepancy at the maximum is 17%. These large values may be caused in part by the probe averaging the field.

Comparison of the phase data in Figures 5.1-8 and 5.1-12 shows smaller discrepancies for $E_z \neq 0$ than for $E_z \neq 0$. The intensity discrepancies are smaller for $E_z \neq 0$ near the maxima and minima, but the computed curves intersect near inflection points.

Comparison of Figures 5.1-9 and 5.1-13 shows smaller phase and intensity discrepancies for $E_z \neq 0$ than for $E_z = 0$.

The theories give the polarization difference, which appears in the differences between the shapes of the phase curves in Figures 5.1-8 and 5.1-12 on the one hand and those in Figures 5.1-9 and 5.1-13 on the other.

Discrepancies seem reasonable in light of the fact that the calculations used only eight cells per ring. The inclusion of E_z seems to improve the theory.

6.   CONCLUSIONS

This project produced several conclusions about electromagnetic waves near dielectric slabs, shells, cylinders, and shells.   These structures are models of radomes, which produce boresight error that degrades the operation of avionic systems and guidance systems.

The report gives specific experimental and numerical evidence for guided waves on slabs and axially symmetric shells.   Such waves are omitted in conventional radome analysis. However, they have significant influence on broadband systems.   They influence transmittance and boresight error, and are polarization dependent.

The report describes an extension of the moment method.   Although our theory is based on Richmond's vector and scalar potential approach, we did analysis for a new decomposition of curved shells and derived closed form expressions for matrix elements without appealing to regular shapes or infinite sizes of cells.   Moreover, the theory treated polarization by including both axial and radial field components.   The addition of the axial component complicated the theory.

Experiments with cylinders and cones tested the accuracy of nearfield calculations. Discrepancies between experiment and calculation were the criteria.   Small discrepancies were produced by the theory that included both axial and radial components even for off-axis incidence.   Discrepancies were appreciable for a version of the theory that had only two radial fields.

7. REFERENCES

1. R. A. Hayward, E. L. Rope, G. Tricoles, "Accuracy of Two Methods for Radome Analysis," Digest 1979 IEEE A-P Society Symposium, pp. 598-601.

2. G. Tricoles, R. A. Hayward, E. L. Rope, "Measurement Calculation, and Reduction of Radome Wave Aberrations," IEEE Antennas and Propagation Symposium Digest, June 1981, pp. 602-607. IEEE Catalog No. 81CH1672-5.

3. G. Tricoles, E. L. Rope, R. A. Hayward, General Dynamics Electronics Division Report R-82-042 March 1982, First Quarterly Report for Contract N00019-81-C-0389.

4. G. Tricoles, R. A. Hayward, E. L. Rope, "Self-Referencing Guidance Interfer-ometer," General Dynamics Electronics Division Report R-80-029-F, June 1980.

5. G. Tricoles, E. L. Rope, and R. A. Hayward, "Wave Propagation Through Axially Symmetric Dielectric Shells," General Dynamics Electronics Division Report R-81-125, June 1981.

6. J. H. Richmond, "Scattering by a Dielectric Cylinder of Arbitrary Cross Section Shape," IEEE Trans., Vol. AP-13, pp. 334-341 (1965).

7. J. H. Richmond, "TE-wave Scattering by a Dielectric Cylinder of Arbitrary Cross Section Shape," IEEE Trans., Vol. AP-14, pp. 460-464 (1966).

8. R. F. Harrington, Time Harmonic Electromagnetic Fields, McGraw-Hill (1961), pp. 163-168.

9. R. A. Hayward, E. L. Rope, G. Tricoles, "Numerical Analysis of Radome Boresight Error," General Dynamics Electronics Division Report R-77-108, December 1977.

END

DATE
FILMED

10 — 83

DTIC